

Electron energy deposition in an e-beam pumped KrF amplifier: impact of beam power and energy

G. M. Petrov

Berkeley Scholars, Inc., P.O.Box 852, Springfield, VA 22150

J. L. Giuliani, and A. Dasgupta

Plasma Physics Division, Naval Research Laboratory, Washington, DC 20375

(December 23, 2002)

Abstract

The electron deposition in an Ar-Kr-F₂ mixture, based on solution of the electron Boltzmann equation, is presented. The model is relevant to an e-beam generated KrF* laser amplifier at atmospheric pressure. Sets of cross sections for Ar, Kr and F₂ have been compiled. Calculations have been performed to determine the electron energy distribution function, energy per electron-ion pair and the ionization and excitation rates. It is found that inclusion of inner shell ionization and the subsequent Auger emission is essential for matching known results on both the energy per ion-electron pair \mathcal{W}_{ei} and the stopping power in pure Ar or Kr target gases. For the chosen Ar-Kr-F₂ mixture, \mathcal{W}_{ei} is calculated to be 24.6 eV. The excitation-to-ionization ratio is calculated to be 0.38 for Ar and 0.54 for Kr at low input power density P_{beam} (1 kW/cm³). Both ratios increase with P_{beam} , particularly for Kr which attains 0.8 at 1 MW/cm³. The dependency on P_{beam} and the excitation efficiency for Kr is significantly higher than previously assumed in KrF* kinetic models. Results are also compared with the Continuous Slowing Down Ap-

Report Documentation Page				Form Approved OMB No. 0704-0188	
Public reporting burden for the collection of information is estimated to average 1 hour per response, including the time for reviewing instructions, searching existing data sources, gathering and maintaining the data needed, and completing and reviewing the collection of information. Send comments regarding this burden estimate or any other aspect of this collection of information, including suggestions for reducing this burden, to Washington Headquarters Services, Directorate for Information Operations and Reports, 1215 Jefferson Davis Highway, Suite 1204, Arlington VA 22202-4302. Respondents should be aware that notwithstanding any other provision of law, no person shall be subject to a penalty for failing to comply with a collection of information if it does not display a currently valid OMB control number.					
1. REPORT DATE 23 DEC 2002		2. REPORT TYPE		3. DATES COVERED 00-00-2002 to 00-00-2002	
4. TITLE AND SUBTITLE Electron energy deposition in an e-beam pumped KrF amplifier: impact of beam power and energy				5a. CONTRACT NUMBER	
				5b. GRANT NUMBER	
				5c. PROGRAM ELEMENT NUMBER	
6. AUTHOR(S)				5d. PROJECT NUMBER	
				5e. TASK NUMBER	
				5f. WORK UNIT NUMBER	
7. PERFORMING ORGANIZATION NAME(S) AND ADDRESS(ES) Naval Research Laboratory, Plasma Physics Division, Code 6730, Washington, DC, 20375				8. PERFORMING ORGANIZATION REPORT NUMBER	
9. SPONSORING/MONITORING AGENCY NAME(S) AND ADDRESS(ES)				10. SPONSOR/MONITOR'S ACRONYM(S)	
				11. SPONSOR/MONITOR'S REPORT NUMBER(S)	
12. DISTRIBUTION/AVAILABILITY STATEMENT Approved for public release; distribution unlimited					
13. SUPPLEMENTARY NOTES					
14. ABSTRACT see report					
15. SUBJECT TERMS					
16. SECURITY CLASSIFICATION OF:			17. LIMITATION OF ABSTRACT Same as Report (SAR)	18. NUMBER OF PAGES 56	19a. NAME OF RESPONSIBLE PERSON
a. REPORT unclassified	b. ABSTRACT unclassified	c. THIS PAGE unclassified			

proximation to demonstrate that this approach is limited to the regime of low power deposition.

PACS: 52.40.Mj, 42.55.Lt, 52.20.Fs, 52.25.Dg

I. INTRODUCTION

The KrF* laser is the highest power and highest efficiency gas laser in the UV region of the spectrum. Based on scaling from laser experiments such as LAM¹, NIKE^{2,3}, ELECTRA⁴, and others⁵, multiple amplifier systems are potential candidates for inertial confinement fusion energy⁶. Large aperture KrF* lasers at near atmospheric pressure are pumped by high power density (hundreds of kW/cm³), high energy (hundreds of KeV) electron beams. The deposition of the electron energy occurs primarily through inelastic collisions with the Ar and Kr gases in the amplifier, since F₂ is a minor constituent. The ionization and excitation rates of the rare gas (Rg) species produced by the beam deposition are essential input for modeling the gas kinetics of the amplifier⁷⁻¹¹. The direct formation of the KrF* exciplex proceeds by ionic recombination ($\text{Kr}^+ + \text{F}^- \rightarrow \text{KrF}^*$) and the harpoon reaction ($\text{Kr}^* + \text{F}_2 \rightarrow \text{KrF}^* + \text{F}$). Furthermore, Rg* and Rg⁺ initiate reactions leading to other excimers and formation pathways (e.g., $\text{ArF}^* + \text{Kr} \rightarrow \text{KrF}^* + \text{Ar}$). The ionization rate for a rare gas species by an e-beam is given by $P_{beam}/[N_{Rg}\mathcal{W}_{ei}(\text{Rg})]$, where N_{Rg} is the rare gas density, P_{beam} is the e-beam power density measured in the amplifier by a pressure-jump method⁸, and $\mathcal{W}_{ei}(\text{Rg})$ is the energy per ion-electron pair created. The last quantity has been measured for many pure gases^{12,13}: $\mathcal{W}_{ei} = 26.2$ eV for Ar and 24.3 eV for Kr. On the other hand, the excitation rate is not directly measured but is instead determined from a detailed model of the degradation of beam electrons and all generations of secondary electrons. The excitation rate is often expressed through the number of excitations per ionization.

Peterson and Allen¹⁴ employed the continuous slowing down approximation^{15,16} (CSDA) to estimate the excitation and ionization efficiencies along with the loss function in Ar. The set of phenomenological cross sections for electron impact from the ground state included excitation to various levels as well as valence shell and inner-shell ionization. Because ionization produces a secondary electron, a deposition model also requires the energy differential ionization cross sections, $S^{ion}(\epsilon, u)$, which gives the distribution of energies u for the ejected electron due to ionization by a primary of energy ϵ . $\int S^{ion}(\epsilon, u)du$ equals the total ionization

cross section. By adjusting the width for u in $S^{ion}(\epsilon, u)$ Peterson and Allen were able to generate a loss function that agrees with the stopping power in Ar at 10 keV from Berger and Seltzer¹⁷. However $\mathcal{W}_{ei}(\text{Ar})$ was found to be too large, 29.0 eV, and it was suggested that the discrepancy may be due to the nature of the CSDA. Summing all the excitation efficiencies from their results one finds that the excitation-to-ionization ratio for Ar is ~ 0.28 . Based on the similarity of the electronic structure between Ar and Kr, Lorents¹⁸ surmised that the excitation-to-ionization ratio for Kr is ~ 0.35 . Since this work all models for the KrF* kinetics in e-beam pumped amplifiers have adopted excitation ratios for Ar and Kr between 0.28 and 0.35, independent of the beam power density.

A more general approach for the ionization and excitation rates produced by an e-beam is to evaluate them from the electron energy distribution function (EEDF). Bretagne, *et al.*¹⁹ determined the EEDF for an Ar target gas above the lowest threshold energy (11.56 eV) using a reduced Boltzmann equation which neglected electron-neutral and Coulomb collisions between electrons. The processes included in their degradation model were excitation, with the same cross sections as given by Peterson and Allen, and valence shell ionization, but not inner-shell ionization. The form used for the energy differential ionization cross section for the valence shell was based on the analytic expression of Green and Sawada²⁰ and fitted to the experimental data of Vroom, *et al.*²¹. It is narrower than the function used by Peterson and Allen and the total ionization cross section is smaller, in better agreement with data for Ar²². The calculated value for $\mathcal{W}_{ei}(\text{Ar})$ was 25.4 eV, close to the observed one, but no comparison with the Ar stopping power was presented. Using Bretagne, *et al.*'s cross sections we find that the resultant loss function is a factor of 2 smaller than the Ar stopping power of Berger and Seltzer. From the branching ratios presented by Bretagne, *et al.*, one finds an excitation-to-ionization ratio for Ar of ~ 0.35 , noticeably higher than calculated by Peterson and Allen.

Other analyses of the e-beam degradation in rare gases have been performed but the excitation-to-ionization ratio was not evaluated or was based on only a couple of excitation channels. The continuous nature of the CSDA can be amended to account for the discrete

energy loss in each inelastic collision¹⁵ by using the Fowler equation²³ or a Monte Carlo calculation²⁴. Dayashankar²³ examined the ionization yield in Kr due to an e-beam and recovered $\mathcal{W}_{ei}(\text{Kr}) = 23.6$ eV. Inner shell ionization and the Auger effect were included. Elliot and Green²⁵ considered the EEDF in a beam generated Ar plasma, including Coulomb collisions between electrons, impact excitation to the lumped 4s and 3d configurations, and the energy range below 11.56 eV. Notably, the EEDF was found to be Maxwellian below the lowest excitation threshold but the tail above the ionization energy is depleted. This is relevant to KrF* kinetics since some models have treated the deposition as producing a beam component for the fast electrons superimposed over a pure Maxwellian distribution for the bulk electrons⁹. This approximation can overestimate ionization by the bulk component if the mean energy of the bulk electrons is several eV.

There are thus significant reasons to reinvestigate the ionization and excitation rates produced in an e-beam generated plasma as applied to KrF* amplifiers. (i) At present an inconsistency exists between the degradation models: the CSDA of Peterson and Allen agrees with the Ar stopping power but not the measured energy per ion-electron pair, while the opposite occurs for the reduced Boltzmann model used by Bretagne, *et al.* (ii) The Kr excitation efficiency in a KrF* mixture has not been analyzed, even though Kr is obviously an essential constituent and has a lower excitation threshold than Ar. (iii) Improved cross sections for electronic excitations of both Ar and Kr are available from experiments^{26,27} and theory²⁸. (iv) A Boltzmann solution for the excitation-to-ionization ratio including many excited states, elastic scattering for the low energy component, and a self-consistent treatment of the electron density is lacking.

In the present paper, we solve the steady state, spatially independent, electron Boltzmann equation from the beam energy down to 0 eV to study the ionization and excitation rates in a beam generated Ar-Kr-F₂ plasma (68.5% Ar, 31% Kr, 0.5% F₂). A nearly complete set of cross sections are presented for electron-neutral elastic scattering, excitation (from new data), valence and inner shell ionizations, as well as Coulomb collisions between electrons for relaxation. The electron energy distribution function, mean energy of the bulk

electrons and density, branching ratios for various energy channels, energy per electron-ion pair, and loss function are investigated at different beam powers and beam energies for the chosen mixture. The electron Boltzmann equation accounts for relaxation of the distribution function around the excitation threshold which is important at high electron densities ($n_e \sim 10^{14} \text{ cm}^{-3}$)^{29–33}. The trend toward Maxwellianization enhances excitation but not ionization, and cannot be modeled by the CSDA. In addition, in Kr/Ar mixtures the EEDF responds to the lower excitation threshold of Kr and the excitation rates of Kr are affected. The CSDA is appropriate only at low electron densities, where electron Coulomb collisions can be neglected.

Investigations based on solution of the electron Boltzmann equation for laser amplifiers have also not addressed inner shell ionization and the production of Auger electrons. Although the probability for inner shell ionization is smaller than valence shell ionization, it is important to the electron power loss, and the resultant Auger electrons are born with plenty of energy for further ionizations. By including these processes we have found reasonable agreement with both the data for the energy per ion-electron pair and the stopping power in pure Ar and Kr target gases. Our results indicate that the excitation-to-ionization ratios are ~ 0.38 for Ar and 0.54 for Kr for the chosen mixture. Furthermore, both ratios are found to increase with beam power density due to the increase in n_e . This is especially true for Kr, which ratio rises to 0.8 at 1 MW/cm^3 .

The paper is organized as follows. The electron Boltzmann equation and its solution are discussed in Section II. Section III contains a discussion of the cross sections used in the analysis. The results of the electron beam deposition for different beam conditions are presented in the next section and a summary concludes the report.

II. ELECTRON ENERGY DEPOSITION MODEL

A. The electron Boltzmann equation

The electron energy distribution function is a key characteristic in every simulation procedure regarding discharge kinetics and the correct description of the plasma properties require its calculation in every particular case. It is well recognized that the electron distribution function in an e-beam generated plasma possesses a complex structure. Due to the presence of high energy (keV) beam electrons the EEDF extends to energies equal to that of the beam electrons. The EEDF is obtained by solving the steady state, electron Boltzmann equation for a plasma sustained by an uniform e-beam. The collisional processes considered include elastic collisions (electron-atom and electron-molecule), Coulomb collisions, as well as inelastic collisions (vibrational excitation, excitation to electronically excited states, attachment to F_2 molecules and ionization). Only processes with ground state atoms and molecules are considered here. Without an external electric field, the electron Boltzmann equation in cgs units can be written in form²⁵:

$$\begin{aligned}
\frac{\partial f}{\partial t} = 0 = & -\frac{\partial}{\partial u} \left[\sum_{\alpha} \frac{2m}{M_{\alpha}} \sigma_a^{mom}(u) v(u) N_{\alpha} \left((T_g/2 - u) f(u) - T_g u \frac{\partial f(u)}{\partial u} \right) \right] \\
& -\frac{\partial}{\partial u} \left[\frac{2\pi e^4}{3} \left(\frac{2}{m} \right)^{1/2} \ln(L) \left(P(u) \left(\frac{f(u)}{2u} - \frac{\partial f(u)}{\partial u} \right) - Q(u) f(u) \right) \right] \\
& + \sigma^{vib}(u + U^{vib}) v(u + U^{vib}) N_{F_2} f(u + U^{vib}) - \sigma^{vib}(u) v(u) N_{F_2} f(u) \\
& + \sigma^{dis}(u + U^{dis}) v(u + U^{dis}) N_{F_2} f(u + U^{dis}) - \sigma^{dis}(u) v(u) N_{F_2} f(u) \\
& + \sum_{\alpha} \sum_{\ell} \left[\sigma_{\alpha,\ell}^{exc}(u + U_{\alpha,\ell}^{exc}) v(u + U_{\alpha,\ell}^{exc}) N_{\alpha} f(u + U_{\alpha,\ell}^{exc}) - \sigma_{\alpha,\ell}^{exc}(u) v(u) N_{\alpha} f(u) \right] \\
& + \sum_{\alpha} \sum_k \left[\int_{u+U_{\alpha,k}^{ion}}^{2u+U_{\alpha,k}^{ion}} S_{\alpha,k}^{ion}(\epsilon, \epsilon - U_{\alpha,k}^{ion} - u) v(\epsilon) N_{\alpha} f(\epsilon) d\epsilon \right. \\
& \left. + \int_{2u+U_{\alpha,k}^{ion}}^{\infty} S_{\alpha,k}^{ion}(\epsilon, u) v(\epsilon) N_{\alpha} f(\epsilon) d\epsilon - \sigma_{\alpha,k}^{ion}(u) v(u) N_{\alpha} f(u) \right] \\
& + R^{beam} \psi^{beam}(u) + \sum_{\alpha} R_{\alpha}^{auger} \psi_{\alpha}^{auger}(u) - \sigma^{att}(u) v(u) N_{F_2} f(u) .
\end{aligned} \tag{1}$$

The energy distribution of the plasma electrons $f(u)$ is normalized according to $n_e = \int_0^\infty f(u)du$. T_g is the gas temperature in energy units, m and e are the mass and magnitude of electron charge, respectively, and $v(u)$ is the absolute value of the electron velocity with kinetic energy u . Furthermore, M_α , N_α , and $\sigma_\alpha^{mom}(u)$ are the mass, density and the momentum transfer cross section of heavy particle α =Ar, Kr and F₂.

The first term in the right hand side of Eq. (1) is the flux of electrons along the energy space driven by elastic electron-neutral collisions. The second term represents Coulomb collisions between electrons using the conventional Fokker-Planck expression with the two integral terms $P(u) = 2u^{-1/2} \int_0^u \epsilon f(\epsilon) d\epsilon + 2u \int_u^\infty \epsilon^{-1/2} f(\epsilon) d\epsilon$ and $Q(u) = 3u^{-1/2} \int_0^u f(\epsilon) d\epsilon$. $\ln(L)$ is the Coulomb logarithm, where $L = \left(\frac{k_B T_e}{4\pi n_e e^2}\right)^{\frac{1}{2}} \frac{mv_0^2}{2e^2}$, k_B is the Boltzmann constant, T_e and n_e are the electron temperature and density respectively and v_0 is the magnitude of the electron velocity. Excitation to the ℓ -th level of species α from the ground state is characterized by the cross section $\sigma_{\alpha,\ell}^{exc}(u)$ and energy threshold $U_{\alpha,\ell}^{exc}$. In addition, several collision processes with F₂ molecules are taken into account: vibrational excitation (upper index "vib"), dissociation (upper index "dis") and attachment (upper index "att"). For simplicity the first two processes are described with a lumped cross section.

After an ionization event the available kinetic energy is shared between the scattered and secondary electrons. The first integral term of Eq. (1) accounts for the scattered primary electrons which reenter the distribution at energy u as a result of ionizing collisions by electrons with incident energies between $u + U_{\alpha,k}^{ion}$ and $2u + U_{\alpha,k}^{ion}$, while the second integral term accounts for all the secondary electrons which reenter the distribution at energy u as a result of ionizing collisions by primary electrons with energies between $2u + U_{\alpha,k}^{ion}$ and ∞ . The third term describes the electrons leaving the distribution at energy u as a result of ionizing collisions. The index $k = v, i$ is summed over the valence shell v (M-shell for Ar and N-shell for Kr) and inner shell i (L-shell for Ar and M-shell for Kr) ionization processes. Each ionization is characterized by an energy differential cross section $S_{\alpha,k}^{ion}(\epsilon, u)$, in which a primary electron with energy ϵ creates a secondary electron with energy u . The

ionization from shell k of species α has a threshold of $U_{\alpha,k}^{ion}$ and a total ionization cross section $\sigma_{\alpha,k}^{ion}(\epsilon) = \int_0^{T_{\alpha,max}} S_{\alpha,k}^{ion}(\epsilon, u) du$. $T_{\alpha,max} = (\epsilon - U_{\alpha,k}^{ion})/2$ is the maximum energy of the secondary electron.

The next term describes ionization by the beam electrons which enter the plasma with energy U_{beam} . The distribution of the beam electrons may come from experiment or other theoretical considerations, but in most practical cases it does not play significant role. To imitate a monoenergetic electron beam, we prescribe a Gaussian profile for the e-beam distribution $\psi^{beam}(u) = (\pi u_w)^{-1/2} e^{-(u-U_{beam})^2/u_w^2}$, with normalization $\int_0^\infty \psi^{beam}(u) du = 1$. The width of the energy distribution, u_w , is assumed to be much smaller than the beam energy itself and in all calculations we used $u_w = 0.01 U_{beam}$. The ionization rate R^{beam} by the beam electrons is calculated from the power deposition in the plasma (see subsection B).

The flux of Auger electrons with energy u appearing due to Auger emission from species $\alpha = \text{Ar, Kr}$ is treated as source term in Eq. (1). R_α^{auger} and ψ_α^{auger} are the rate and the energy distribution of the appearing electrons, respectively. The latter is assumed to be monoenergetic and is described as a narrow Gaussian profile $\psi_\alpha^{auger}(u) = (\pi u_w)^{-1/2} e^{-(u-U_\alpha^{auger})^2/u_w^2}$, with normalization $\int_0^\infty \psi_\alpha^{auger}(u) du = 1$. The energy of the Auger electrons is U_α^{auger} and $u_w = 5\text{eV}$ is the width of the energy distribution.

B. Electron and power balance equations

The relevant electron macroscopic balance equations are derived by appropriate energy space averaging of the electron Boltzmann Eq. (1). The time dependence of $f(u)$ can be neglected since the characteristic time for establishment of steady state distribution is of order of few ns¹⁹, which is two orders of magnitude smaller than the electron beam duration in large aperture lasers.³ Integration of Eq. (1) with respect to the kinetic energy from zero to infinity leads to the electron particle balance equation:

$$R_{tot}^{ion} = \sum_\alpha (R_{\alpha,v}^{ion} + R_{\alpha,i}^{ion}) + \sum_\alpha R_\alpha^{auger} + R^{beam} = R^{att} . \quad (2)$$

Here the ionization rates from the valence shell ($R_{\alpha,v}^{ion}$) and the inner shell ($R_{\alpha,i}^{ion}$) from species α have been denoted separately. R_{α}^{auger} is the Auger electron production rate from the same species and R^{att} is the attachment rate to F_2 molecules. These values are given by the following expressions:

$$\begin{aligned}
R_{\alpha,v}^{ion} &= \int_0^{\infty} \sigma_{\alpha,v}^{ion}(u) v(u) N_{\alpha} f(u) du \\
R_{\alpha,i}^{ion} &= \int_0^{\infty} \sigma_{\alpha,i}^{ion}(u) v(u) N_{\alpha} f(u) du \\
R_{\alpha}^{auger} &= R_{\alpha,i}^{ion}, \\
R^{beam} &= P_{beam}/U_{beam} \\
R^{att} &= \int_0^{\infty} \sigma^{att}(u) v(u) N_{F_2} f(u) du .
\end{aligned} \tag{3}$$

The Auger yield from an inner shell ionization is taken as unity^{24,34}. The ionization rate R^{beam} by the external electrons is calculated from the power deposition in the plasma. The attachment to F_2 molecules is the only electron loss process considered. Another potential electron loss mechanism is dissociative recombination with Ar_2^+ , Kr_2^+ and F_2^+ , but the attachment rate is more than an order of magnitude larger compared to the dissociative recombination rate. It should be mentioned that the electron particle balance Eq. (2) is used to constrain the normalization of $f(u)$ and is thus treated as an independent relation, even though it follows in principle from Eq. (1).

Multiplication of Eq. (1) by the kinetic energy u , followed by integration with respect to the kinetic energy from zero to infinity leads to the power balance equation,

$$P_{beam} = P^{vib} + P^{dis} + P^{att} + \sum_{\alpha} \left[P_{\alpha}^{el} + P_{\alpha,\ell}^{exc} + P_{\alpha,v}^{ion} + (P_{\alpha,i}^{ion} - P_{\alpha}^{auger}) \right] . \tag{4}$$

The electron power gain or loss terms are defined as

$$\begin{aligned}
P^{vib} &= U^{vib} \int_0^{\infty} \sigma^{vib}(u) v(u) N_{F_2} f(u) du \\
P^{dis} &= U^{dis} \int_0^{\infty} \sigma^{dis}(u) v(u) N_{F_2} f(u) du \\
P^{att} &= \int_0^{\infty} \sigma^{att}(u) v(u) N_{F_2} u f(u) du
\end{aligned}$$

$$\begin{aligned}
P_{\alpha}^{el} &= \frac{2m}{M_{\alpha}} \int_0^{\infty} \sigma_{\alpha}^{mom}(u) v(u) N_{\alpha} \left((T_g/2 - u) f(u) - T_g u \frac{df(u)}{du} \right) \\
P_{\alpha,\ell}^{exc} &= U_{\alpha,\ell}^{exc} \int_0^{\infty} \sigma_{\alpha,\ell}^{exc}(u) v(u) N_{\alpha} f(u) du \\
P_{\alpha,v}^{ion} &= U_{\alpha,v}^{ion} R_{\alpha,v}^{ion}, \quad P_{\alpha,i}^{ion} = U_{\alpha,i}^{ion} R_{\alpha,i}^{ion}, \quad P_{\alpha}^{auger} = U_{\alpha}^{auger} R_{\alpha}^{auger} .
\end{aligned} \tag{5}$$

The electron power gain comprises two terms, that due to beam electrons P_{beam} and due to Auger electrons P_{α}^{auger} . For convenience, the latter is transferred in the right hand side of the equation. The first, second, and third terms on the right represent power loss in vibrational excitation, dissociation and attachment to F_2 molecules, respectively. The first term within the sum describes the power loss in elastic electron-atom or electron-molecule collisions. Then follows the power loss in excitation of Ar, Kr and F_2 , the power loss in valence and finally inner shell ionizations. The power balance of electrons in Eq. (4) is not an independent equation since it follows directly from Eq. (1). It is automatically fulfilled by a properly normalized solution to the Boltzmann equation.

C. Boundary conditions

Equation (1) is an integro-differential equation and it must be accompanied with boundary conditions. At energy U_{max} , slightly exceeding the beam energy, the electron distribution function is set to zero. The high-energy part of the EEDF is calculated accounting for inelastic collisions only. The elastic electron-atom and electron-molecule collisions are neglected due to the small mass ratio and small cross sections at high energy. The Coulomb collisions between electrons have also been neglected since the electron-electron interaction cross section decreases rapidly with increasing the kinetic energy. By neglecting the Coulomb collisions Eq.(1) is no longer an integro-differential equation and $f(u)$ can be directly obtained. The EEDF is calculated backwards, from higher to lower energy, starting with U_{max} and finishing at appropriate energy U^* (=30-40 eV).

The low-energy part of Eq.(1) contains nonlinear terms, namely $P(u)$ and $Q(u)$, and the Coulomb logarithm term $\ln(L)$. The latter depends explicitly on the electron density

and electron temperature. These nonlinear terms and $\ln(L)$ are treated iteratively. For each iteration the low-energy part of the EEDF is calculated and the electron density and mean energy of the bulk electrons are calculated. Then $\ln(L)$ is updated, assuming that the electron temperature is $2/3$ of the mean energy of the bulk electrons. The nonlinear coefficients $P(u)$ and $Q(u)$ are also updated with the newly calculated EEDF and added to the coefficients, resulting from elastic electron-atom and electron-molecule collisions.

At kinetic energy U^* we take $f(U^*)$ from the high-energy calculation of the EEDF. At kinetic energy $u=0$ we take as the boundary condition the normalization of the EEDF in the low energy region, vis., $n_e^* = \int_0^{U^*} f(u)du$. The integral is presented as a sum at each grid point by using, for example, the Simpson's rule. This sum, involving all unknown discrete values of the EEDF in the low energy region, provides the second boundary condition^{35,36}. Equation (1) and the boundary condition at kinetic energy $u = 0$ are reduced to a coupled system of linear algebraic equations with a tri-diagonal matrix, resulting from the discretization of Eq.(1), and an additional first row of non-zero elements, resulting from the discretization of $\int_0^{U^*} f(u)du$. The system of linear algebraic equations is solved by Gaussian elimination of the matrix elements below the diagonal and a backsubstitution.

The boundary condition at kinetic energy $u = 0$ requires the electron density in the low energy region n_e^* to be known, which is derived from the electron particle balance Eq. (2). The left hand side of this equation is not automatically equal to the right hand side and the equality must be enforced. The left hand side depends mostly on the high-energy part of the EEDF ($u > U^*$), while the major contribution to the right hand side comes from the low-energy part of the EEDF ($u < U^*$), which is proportional to n_e^* . Consequently, n_e^* can be adjusted so that the only electron loss process, the attachment rate to F_2 molecules (the right hand side of Eq. (2)), matches the sum of all ionization rates (the left hand side of Eq. (2)). The electron density in the low energy region n_e^* has to be updated after each iteration, since a weak dependence of the ionization rate on the EEDF in the low energy region still exists. It should be noted that the total electron density n_e is calculated by integration of the EEDF in the entire energy region. Since the tail of the EEDF is several

orders of magnitude smaller compared to the low energy part of the EEDF, n_e^* is only slightly smaller than n_e . An advantage of implementing such a procedure is that the electron particle balance condition relaxes smoothly during convergence.

D. Auger ionization

The inner shell ionization cross section of Ar is about two orders of magnitude smaller compared to the valence shell ionization cross section. It increases the number of ionizations by only about 1-2%; however, due to its high energy threshold it contributes significantly to the power loss, of order of 10-15%. This has a remarkable impact on the energy per electron-ion pair, since the inner shell ionization is an additional power sink while having negligible increase of the ionization rate. Estimations show that the energy per electron-ion pair may increase by about 5 eV only due to the inner shell ionization and become 30 eV and higher. For comparison, 26.2 eV per electron-ion pair for Ar and 24.3 eV for Kr have been experimentally observed. Thus the inner shell ionization would result in excessively high energy per electron-ion pair, unless a counter effect reduces it.

The Auger effect arises from the internal absorption of the radiative decay from an outer electron shell to the inner shell vacancy formed after an inner shell ionization. The ejected Auger electron from the L-shell of Ar or the M-shell of Kr has an energy of $\sim 10^2$ eV which provides an additional source of secondary electron production. This compensates the power loss from inner shell ionization.

As an important ionization channel, the Auger ionization is included in the electron Boltzmann equation. Two parameters are needed: the energy of the Auger electrons and the rate at which they appear. If the energy of the emitted Auger photon is assumed to be equal to the energy of inner shell ionization, and the final state of the atom is a doubly ionized ion (two electrons have been ejected, one directly and one Auger), the energy of the Auger electron is the energy difference between the energy of inner shell ionization and the energy of double ionization, which for Ar and Kr is of order 40 eV.

In spite of the complex nature of the phenomenon, it is fairly simple to treat the Auger electrons in the electron Boltzmann equation. Keeping in mind that $f(u)$ is calculated backwards, from higher to lower energies, the rate for inner shell ionization can be calculated immediately after the kinetic energy becomes equal to the ionization threshold ($U_{Ar,L}^{ion} = 247$ eV and $U_{Kr,M}^{ion} = 91$ eV). Since the Auger electrons appear at lower energies ($U_{Ar,L}^{Auger} = 202$ eV and $U_{Kr,M}^{Auger} = 50$ eV), the term accounting for Auger ionization in Eq. (1) is known because the rate for inner shell ionization has already been calculated.

III. ATOMIC DATA

A. Argon

Electron impact cross sections for Ar, Kr and F₂ are essential for solving Eq.(1). Compilations of cross sections for use in various Ar plasma models have been gathered since the early 70's (Refs. ^{14,37-39}). The excitation cross sections to individual levels or group of levels adopted in the present work are shown in Fig. 1a and b, and presented as analytic fits in Table I. Cross sections to the four levels of the 4s configuration has either been measured⁴⁰⁻⁴² or computed^{28,39,43-45} and we have used the results from Ref.²⁸. Individual^{26,28,45-47} and lumped^{39,40,44} excitation cross sections from the ground state to the ten 4p levels are optically forbidden and the cross sections exhibit different behavior. After passing through a maximum, some of the cross sections fall off slowly, $\propto u^{-1}$, while the fall-off behavior of others is rather sharp, $\propto u^{-3}$. A reasonable approximation is to divide the levels into two groups according to their behavior at high energy and use the summed cross section for each group. They are referred to as Ar(4p)⁽¹⁾ and Ar(4p)⁽²⁾. Excitation to the 3d configuration of Ar is accounted for as a sum of forbidden and allowed cross sections. The optically forbidden transitions have been measured⁴⁸ but no data are available for the allowed ones. We used the Drawin's formula⁴⁹ for the latter excitations:

$$\sigma_{Ar,\ell}(u) = 4\pi a_0^2 (R_y / U_{Ar,\ell}^{exc})^2 f_{g,\ell}(x - 1) \ln(1.25x) x^{-2}. \quad (6)$$

Here ℓ represents the $3d$ configuration with excitation energy $U_{Ar,\ell}^{exc}$ and oscillator strength from the ground state $f_{g,\ell}$. Also a_0 is the Bohr radius and R_y is Rydberg's constant. $x = u/U_{Ar,\ell}^{exc}$ is the electron's energy relative to the excitation energy. Excitation to the $5s$ configuration is treated in the same fashion. We have estimated the excitation cross section for the $5p$ configuration according to scaling laws of Sobelman⁵⁰. Applying this scaling to the $4p$ and $5p$ states of Ar, one has

$$\frac{\sigma_{Ar,5p}^{exc}}{\sigma_{Ar,4p}^{exc}} = \left(\frac{U_{Ar,4p}^{exc}}{U_{Ar,5p}^{exc}} \right)^2 \left(\frac{U_{Ar,M}^{ion} - U_{Ar,5p}^{exc}}{U_{Ar,M}^{ion} - U_{Ar,4p}^{exc}} \right)^{3/2}, \quad (7)$$

where $U_{Ar,M}^{ion}$ is the valence shell ionization potential of Ar. Three other groups of levels are considered in the model: $Ar(4d)$, $Ar(6s)$ and Ar^{**} . The latter comprises all cross sections between the $6s$ configuration and the continuum. The electron impact excitation cross section to each of these configurations is calculated using Eq. 6 with oscillator strengths from⁵¹. In summary, the set of cross sections for electron impact excitation of Ar comprises 12 cross sections, which should describe fairly accurately the energy deposition in excitation processes.

The summed cross section for all excitations of Ar is displayed in Fig. 2 along with the momentum transfer, valence (M) and inner (L) shell ionization cross sections. The momentum transfer data for Ar is taken from Ref.⁵². The valence shell differential ionization cross section $S_{Ar,M}^{ion}$ for energies of the primary electron up to 500 eV has been tabulated by Opal, *et al.*⁵³. Green and Sawada²⁰ and Peterson and Allen¹⁴ proposed analytical formulae. The best match to the experimental data by Vroom *et al.*²¹ is Bretagne's¹⁹ parameters for the formula of Green and Sawada:

$$S_{Ar,M}^{ion}(\epsilon, u) = A(\epsilon) \frac{\Gamma^2}{(u - u_0)^2 + \Gamma^2}, \quad (8)$$

with $A(\epsilon) = 2.65 \times 10^{-15} \ln(\epsilon/U_{Ar,M}^{ion})/\epsilon$, $u_0 = 1.2 - 250/(\epsilon + 2U_{Ar,M}^{ion})$, $\Gamma = 4.6$ and $U_{Ar,M}^{ion} = 15.75$. The total ionization cross section $\sigma_{Ar,M}^{ion}(\epsilon)$, obtained by integration of the differential ionization cross section Eq. 8, is in excellent agreement with experimental data^{22,54,55}.

The only inner shell differential ionization cross section $S_{Ar,L}^{ion}$ used in calculations of the electron energy spectra is that suggested by Peterson and Allen¹⁴. We believe their guess is

too small based on scaling laws for inner shell ionization by McGuire⁵⁶. Our adopted form is given by

$$S_{Ar,L}^{ion}(\epsilon, u) = \sigma_{Ar,L}^{ion}(\epsilon) \left[\frac{1}{\tan^{-1}(\Gamma/T_{max})} \frac{\Gamma}{u^2 + \Gamma^2} \right], \quad (9)$$

where $\Gamma = 160$ eV. The choice of the width Γ is discussed in subsection D. The energy dependence of $\sigma_{Ar,L}^{ion}(\epsilon)$ is chosen to match McGuire's results. A reasonable fit of the latter is given by $\sigma_{Ar,L}^{ion}(\epsilon) = 6.8 \times 10^{-18} (x - 1) \ln(x)/x^2$, where $x = \epsilon/U_{Ar,L}^{ion}$.

B. Krypton

The set of individual excitation cross sections employed in this work is displayed in Fig. 3a and b and presented as analytic formula in Table II. The set of excitation cross sections for Kr follows the analogous level structure used for Ar. Electron impact excitation cross sections to individual levels in the $5s$ configuration^{27,40,57–59} and lumped^{27,40,60,61} $5p$ states are known, but not to higher states. For the levels in the $5s$ and $5p$ configurations we have used results from a semi-relativistic distorted wave calculation⁶². The oscillator strengths to the $4d$ and $5d$ configurations are enormous, of order of unity, which suggests excessively large cross sections. We have used *effective* oscillator strengths measured from energy loss spectra⁶³, rather than optical oscillator strengths.

The summed cross section for all excitations of Kr is displayed in Fig. 4 along with the momentum transfer, valence (N) and inner shell (M) ionization cross sections. The momentum transfer data is again taken from Ref.⁵². We adopted the differential cross section for valence shell ionization of Kr from Green and Sawada²⁰, as given by Eq. (8), with the fitting parameters: $A(\epsilon) = 1.87 \times 10^{-15} \ln(\epsilon/8.43)/\epsilon$, $u_0 = 3.9 - 1000/(\epsilon + 2U_{Kr,N}^{ion})$, $\Gamma = 7.95\epsilon/(\epsilon - 13.5)$ and $U_{Kr,N}^{ion} = 14.0$ eV. The inner shell differential ionization cross section is calculated in the same manner as for Ar through Eq. (9). The width of the secondary electrons is assumed to be $\Gamma = 60$ eV. The total ionization cross section has been taken from Ref.⁵⁶ and fitted with the function $\sigma_{Kr,M}^{ion}(\epsilon) = 5.5 \times 10^{-17} (x - 1) \ln(1.25x)/(x^2 + 5)$, where $x = \epsilon/U_{Kr,M}^{ion}$.

C. Fluorine

Even though the fractional abundance of fluorine is low in a KrF* amplifier the inelastic collisions of electrons with fluorine is important for determining the low energy (\sim few eV) component of the EEDF and for the disappearance of electrons through attachment. The cross sections compiled by Hayashi and Nimura⁶⁴ for F₂ are adopted for this paper and shown in Fig. 5. Another compilation can be found in Ref.⁶⁵. Four vibrational excitation cross sections are lumped as one effective cross section. Excitation to electronic states $a^3\Pi_u$ (threshold 3.16 eV) and $A^1\Pi_u$ (threshold 4.34 eV), leading to dissociation of the fluorine molecule, are lumped together due to their close thresholds. Likewise for the excitations to $C^1\Sigma_u^+$ (threshold 11.57 eV) and $H^1\Pi_u$ (threshold 13.08 eV). Such a lumping will not affect the electron distribution function.

The valence shell differential ionization cross section of F₂ is not available. We have adopted the differential cross section of N₂ from Green and Sawada²⁰, which has the closest ionization potential to that of F₂. The parameters for Eq. (8) are $A(\epsilon) = 2.28 \times 10^{-16} \ln(\epsilon/1.74)/\epsilon$, $u_0 = 4.71 - 1000/(\epsilon + 2U_{F_2}^{ion})$, $\Gamma = 13.8\epsilon/(\epsilon + U_{F_2}^{ion})$ and $U_{F_2}^{ion} = 15.69$. The coefficient A has been reduced by a factor 3 from the value for N₂ in order to better match the total ionization cross section compiled by Hayashi and Nimura⁶⁴. The inner shell ionization of F₂ has been neglected.

D. Loss function

The analysis of the cross sections continues with the construction of the loss function¹⁴

$$L(\epsilon) = \sum_{\alpha} \sum_{\ell} \sigma_{\alpha,\ell}^{exc}(\epsilon) U_{\alpha,\ell}^{exc} + \sum_{\alpha} \sum_k \int_0^{(u - U_{\alpha,k}^{ion})/2} (U_{\alpha,k}^{ion} + u) S_{\alpha,k}^{ion}(\epsilon, u) du. \quad (10)$$

The first sum is over all discrete excited states and the second sum is over both the valence and inner shell ionization states of all species α . The loss function depends mostly on the cross section for valence shell ionization, but a substantial contribution comes from the inner shell. For both shells the differential ionization cross section $S_{\alpha,k}^{ion}(\epsilon, u)$ falls off rapidly for

$u > \Gamma$ and the integral in the loss function varies roughly as $(U_{\alpha,k}^{ion} + \Gamma/2)\sigma_{\alpha,k}^{ion}(\epsilon)$. Hence the width of the differential ionization cross section Γ is important for the accurate description of the loss function. Γ is only known for the valence shell ionization and there is no information in the literature regarding the width of the inner shell differential ionization cross section. Peterson and Allen¹⁴ assumed that it is 40 eV for Ar, but since the width of the valence shell differential ionization cross section is ~ 10 eV¹⁹, approximately 2/3 of the ionization potential, the width of the inner shell differential ionization cross section may be as large as 160 eV.

One can use the electron stopping power for pure target gases to examine the role of this width. Using the above cross sections we calculated the Ar and Kr loss function for three cases: (A) omitting inner shell ionization; (B) using an differential ionization cross section with width $\Gamma = 40$ eV; and (B') with width 160 eV. The results are presented in Fig. 6a along with the data for the stopping power from Berger and Seltzer¹⁷ calculated using the Born approximation. It is clear that inner shell ionization must be included; curve (A) is well below the stopping power for Ar. The better match with Berger and Seltzer's results for Ar is with a differential ionization cross section having width $\Gamma=160$ eV. The growing difference between curves A, B, and B' and the stopping power beyond ~ 200 eV is due to relativistic effects not included in our cross sections. Similar plots are shown in Fig. 6b for Kr where curves (B) and (B') correspond to widths $\Gamma = 40$ and 60 eV, respectively. The latter value corresponds to 2/3 of the inner M-shell ionization potential for Kr. In the case of Kr the Berger and Seltzer's results can not be reproduced even with the largest width of the inner shell differential ionization cross section. A possible solution may be the inclusion of inner L-shell ionization for Kr.

IV. RESULTS AND DISCUSSION

A. Plasma parameters versus beam power

For the results presented below the target gas is fixed at $N_{Ar} = 1.80 \times 10^{19} \text{ cm}^{-3}$, $N_{Kr} = 8.14 \times 10^{18} \text{ cm}^{-3}$, and $N_{F_2} = 1.25 \times 10^{17} \text{ cm}^{-3}$. This composition is typical for the NIKE KrF* amplifier. The beam power density, P_{beam} , and energy, U_{beam} , are varied to investigate the dependence of the EEDF and excitation rates on these input parameters.

Results for the normalized EEDF $\tilde{f}(u)$ are presented in Fig. 7a as a function of beam power from 1 kW/cm³ to 1 MW/cm³. The beam energy is kept 650 keV regardless of the beam power. The normalized function refers to $\tilde{f}(u) = u^{-1/2} f(u)/n_e$, which for a Maxwellian becomes a straight line in a log-linear plot. The high energy part of the distribution is included in Fig. 7b. At the lowest beam power, 1 kW/cm³, the degree of ionization is only $\sim 10^{-7}$. Below ~ 10 eV the EEDF is primarily formed by elastic scattering with Ar and Kr, attachment and vibrational and electronic excitation with F₂ molecules. In particular, the EEDF turns downwards below ~ 2 eV due to attachment. The cross section for this process increases with decreasing kinetic energy (see Fig. 5). Above 2 eV, the elastic scattering has the opposite effect: it depletes the EEDF as the kinetic energy increases causing $\tilde{f}(u)$ to pass through a maximum. Dissociation causes further depletion of the electron distribution function at kinetic energies of ~ 5 eV. In the energy region between 9 and 14 eV excitation processes with Ar and Kr atoms dominate. The characteristic drop in $\tilde{f}(u)$ at $u \sim 10$ eV is clearly evident and reflects loss of electrons at the first excitation potential of the abundant species Kr (at 9.9 eV) and Ar (at 11.5 eV). Above 14 eV the shape of the EEDF results from the decay of the beam electrons and secondaries by ionization processes.

At input power density of $\sim 100 \text{ kW/cm}^3$ the degree of ionization increases to $\sim 10^{-5}$. The Coulomb and elastic electron-atom collisions with Ar and Kr now affect the EEDF in the low energy region (< 10 eV) and it trends toward a Maxwellian distribution. Nonetheless, even at the highest input power considered, 1 MW/cm^3 , $\tilde{f}(u)$ is still not Maxwellian above

the excitation threshold of Ar. Maxwellization in the whole inelastic region of Ar and Kr can only be achieved at an input power density of several MW/cm³.

The tail of the normalized EEDF is formed by ionization processes with Ar and Kr atoms and decreases as $\sim u^{-1/2}$ in Fig. 7b. The small bumps at 50 eV and 200 eV are due to the appearance of Auger electrons. In spite of the progressively decreasing EEDF and values as small as $\sim 10^{-11}$ at energies $u > 1$ KeV, the tail of the distribution function accounts for $\sim 80 - 90\%$ of the ionizations. However, its contribution to other processes, such as excitation or dissociation of F₂, is negligible. One can conclude that the low- and high-energy parts of the distribution function play distinctive roles in the discharge kinetics: ionization is attributed to the high energy part of the EEDF and all other processes to the low-energy part.

The electron density increases sublinearly with the beam power (Fig. 8a). The mean energy of the bulk electrons $\langle u \rangle = \int_0^{U^*} u f(u) du / n_e$, shown in Fig. 8b, varies by only 10% as the beam power density increases from 1 kW/cm³ to 1 MW/cm³. This variation in $\langle u \rangle$ is due to relaxation of the low energy part of the EEDF resulting from Coulomb collisions between electrons.

With the calculated EEDF, one can readily evaluate the terms of Eq. (5) entering the power balance Eq. (4). Fig. 9 shows the relative variation of these terms with beam power. For simplicity all excitation terms of Ar are summed together and likewise for Kr. The fractional power deposition for most processes depends weakly on the beam power indicating that each term in Eq. (4) increases linearly with P_{beam} . In particular, the Maxwellization of the bulk component of the EEDF with increasing power does not significantly alter the contribution of the various deposition channels, except for Kr excitation which rises from ~ 10 to $\sim 15\%$. For both Ar and Kr, the largest fraction of the power loss is due to valence shell ionization. Excitations contribute about a fourth, while the power losses in both inner shell ionization and elastic collisions account for only few per cent. For inner shell ionization the net power loss is presented, i.e. $P_{Ar,L}^{ion} - P_{Ar}^{Auger}$ and $P_{Kr,M}^{ion} - P_{Kr}^{Auger}$.

The most significant impact of the beam power on the power deposition can be expected

for F_2 , particularly for processes with no threshold (elastic scattering and attachment) or a low energy threshold (vibrational excitation and dissociation). From Fig. 9c the relative power loss in elastic scattering of electrons with F_2 molecules decreases by a factor 3 as the beam power density increases from 1 kW/cm³ to 1 MW/cm³. Over the same increase the relative power loss in F_2 vibrational excitation decreases by about factor two and the relative power loss in attachment decreases by about 50%. The total power loss attributed to F_2 decreases from 12 to 8 per cent and the decrease of power loss of 4% appears as increase of power loss due to electron impact excitation of Kr. Note that even though the fraction of F_2 is only $\sim 0.5\%$, it accounts for $\sim 10\%$ of the total power loss.

Table III lists the individual contributions to the ionization terms of Eq. (3) in the particle balance Eq. (2). The values are normalized by the attachment rate R^{att} . The results are presented at input power of 346 kW/cm³, but they are insensitive with respect to P_{beam} as indicated by Fig. 9. The sum of the valance shell ionizations from Ar, Kr, and F_2 exceeds 90% and dominates the direct contribution from the e-beam electrons. Some results for pure Ar are compared with that of Peterson and Allen, which is discussed in subsection (C).

The energy per electron-ion pair is the ratio of the beam power in Eq. (4) to the total ionization rate in Eq. (2): $\mathcal{W}_{ei} = P_{beam}/R_{tot}^{ion}$. For the chosen composition we find $\mathcal{W}_{ei} = 24.6$ eV, regardless of the beam power. Its variation has been found to be less than 0.1 percent in the entire power deposition range considered. The weak dependence of \mathcal{W}_{ei} versus P_{beam} results as follows. According to Fig. 7b the high energy part of the normalized EEDF \tilde{f} increases with the beam power ($\propto P_{beam}^{0.143}$) while the electron density, as seen from Fig. 8a, increases sublinearly ($\propto P_{beam}^{0.856}$). The resultant ionization rate of Eq. (3), with $f = n_e \sqrt{u} \tilde{f}$, increases linearly with the beam power which leads to the calculated weak dependence of the energy per electron-ion pair of the beam power. We further mention that the energy per electron-ion pair for pure Ar and Kr, calculated with our model, agrees very well with other measurements. We obtained 25 and 24 eV for Ar and Kr respectively, slightly lower than 26 and 24 eV reported in most works.

The branching ratios for energy deposition to individual Ar and Kr levels have also been

investigated. Fig. 10a shows the fractional power loss for each Ar level or group of levels considered in the model. For Ar, only the levels of the $4s$ configuration are affected by the beam power and there is no impact on the deposition channels with energies higher than $4s$. The situation for Kr is different as seen in Fig. 10b: the beam power variation has a strong impact not only on the lowest group of levels, the $5s$ configuration, but also on the two channels leading to the $5p$ configuration. This effect results from the Maxwellianization of the EEDF below ~ 10 eV due to the increase in ionization fraction with P_{beam} and the consequent increased role of the electron Coulomb collisions. Our results differ from Peterson and Allen's, particularly for the $4s$ levels. The excitation rates and energy deposition to the $4s$ levels are larger than Peterson and Allen's results due to the different approach for calculating the electron energy degradation spectra. Further discussion of the deposition rates in pure Ar will be presented in subsection (C).

Consider the sum of all excitation efficiencies for Ar from Fig. 10a and likewise for Kr from Fig. 10b. Upon dividing by the total ionization efficiency one obtains the separate excitation-to-ionization ratios

$$\eta_{\alpha}^{exc} = \frac{\sum_{\ell} R_{\alpha,\ell}^{exc}}{R_{\alpha,v}^{ion} + R_{\alpha,i}^{ion} + R_{\alpha}^{auger}} \quad (11)$$

for $\alpha = \text{Ar, Kr}$ in the specified mixture. These ratios are displayed in Fig. 11 as a function of the beam power. The total ionization rate includes not only valence shell ionizations for both Ar and Kr, but also the contribution from the inner shell and Auger ionization. While the excitation-to-ionization ratio of Ar remains weakly dependent on the beam power density, for Kr it increases from 0.54 at low beam power density to 0.80 at the highest beam power density of 1 MW/cm^3 . Because the energy per ion-electron pair is nearly independent of the beam power, the rise in the Kr excitation efficiency reflects the change seen in the individual levels of Fig. 10b. Peterson and Allen found an excitation-to-ionization ratio for Ar of $\eta_{Ar}^{exc} \approx 0.28$. In KrF kinetic models it has been assumed that a similar ratio holds for Kr. The excitation-to-ionization ratio we compute in a mixture of $68.5\% \text{Ar} + 31\% \text{Kr} + 0.5\% \text{F}_2$ is significantly higher: 0.38 - 0.41 for Ar, and 0.54 - 0.8 for Kr, as the power density increases

from 1 kW/cm³ to 1 MW/cm³.

B. Plasma parameters versus beam energy

In a laser amplifier the choices of the beam energy, target gas pressure, and size are selected to provide a uniform deposition. For example, if either the gas pressure or plasma dimensions increase, the beam energy must also be adequately increased. Too low a beam energy causes nonuniform volume pumping, while an excessive beam energy leads to electrons traversing the plasma without depositing their energy. The determination of the beam energy is often done using the stopping power of Berger and Seltzer¹⁷ which is provided above 10 keV. It is of interest to know whether the EEDF and the deposition channels change with beam energy.

The EEDF for $U_{beam} = 1, 10, 100, 650$ keV and fixed input power (346 kW/cm³) is shown in Fig. 12. The low energy part of the EEDF (below 200 eV) does not depend on the beam energy at all and the electron density and the mean energy of the bulk electrons are found to be independent of the beam energy and their variation with the beam energy is within 0.1%. The high energy part is obviously sensitive to the beam energy, which is the maximum value. Since the extended distribution function for large U_{beam} compensates for the sharp increase in \tilde{f} at low U_{beam} , the ionization rate is independent of the beam energy, as long as the input power is kept the same. Naturally, the energy per ion-electron pair, which is the ratio of the input power to the ionization rate, is also independent of the beam energy. The rates of the other elementary processes are the same within $\sim 1\%$.

In the calculations so far we assumed that the electron beam traversing the plasma is monoenergetic. Since the beam electrons must pass through a foil before entering the KrF amplifier, the beam will emerge into the target gas with possibly a broad energy spectrum. We investigated whether the energy spread of the primary beam affects the energy deposition. The plasma deposition obtained from a monoenergetic beam with $u_w = 0.01U_{beam}$ was compared with ones having much broader energy spectrum of $u_w = 0.1U_{beam}$ and $u_w = 0.3U_{beam}$.

No changes were observed in the EEDF or the rates for elementary processes. We can conclude that, as long as the beam electrons have energies above ~ 10 keV, whether the electron beam entering the plasma is monoenergetic or not is not significant for the energy deposition.

C. Comparison with the continuous slowing down approximation

The CSDA is appropriate in the limit of zero electron density where the thermal relaxation by electron Coulomb or electron-atom elastic scattering does not play a role. Thus one can simulate a discrete version of the CSDA in a Boltzmann model by neglecting Coulomb collisions between electrons. To compare the two approaches, we have solved the Boltzmann equation subject to a fixed degree of ionization: in the first case with a value typical for e-beam deposition (4×10^{-5}) and in the second with a vanishing degree of ionization. Excitation and ionization processes were retained in both cases as well as elastic losses by electron-atom collisions. The CSDA does not truly include these latter collisions, but we included them as part of a modified CSDA to isolate the important effects of Coulomb collisions and to properly describe the EEDF near the lowest excitation threshold.

The EEDF's, calculated by solving the electron Boltzmann equation and the modified CSDA in pure Ar plasma, are shown in Fig. 13a. The beam energy is $U_{beam}=10$ keV. For energies slightly exceeding the threshold for valence shell ionization the solution of the electron Boltzmann equation is the same as the modified CSDA, which explains why the energy per ion-electron pair calculated using the CSDA is in good agreement with Boltzmann models. On the other hand, in the energy region between the first excitation and the ionization thresholds the EEDF is strongly influenced by electron Coulomb collisions. The modified CSDA is inconsistent with the Boltzmann model in this energy region and the electron impact excitation rates cannot be accurately calculated. To better display the difference between the solutions of the CSDA and the electron Boltzmann equation, Fig. 13b shows the ratio of the EEDF's calculated by the modified CSDA and the electron

Boltzmann equation. As it can be seen, the simulated CSDA is very inaccurate between the first excitation threshold and the ionization energy and the deviation from the EEDF computed with the electron Boltzmann equation reaches a factor five. As a consequence, the branching ratios for energy deposition by various Ar excited states differ between the CSDA and the Boltzmann model.

Table IV lists the power deposition in elastic collisions, excitation, valence and inner shell ionization between the two approaches for the EEDF of Fig. 13. Since the EEDF from the CSDA coincides with that calculated from the electron Boltzmann equation above the ionization threshold, the fractional power loss in both valence and inner shell ionization is the same. However, the power loss in elastic collisions calculated from the electron Boltzmann equation is only 5-6%, while the elastic power loss calculated with the modified CSDA is 15-16%, three times larger. The power loss in excitation, as calculated by the CSDA is only 20%, whereas from the Boltzmann model it is about 30%. Thus the modified CSDA tends to overestimate the power loss in elastic collisions and underestimate of the power loss in excitation. The inaccurate power deposition of the CSDA leads to serious implications in the kinetic modelling of a KrF laser amplifier, because a major role in formation of KrF* is played by the electron impact excitation processes.

The differences in the power deposition can be outlined in detail if the results from our Boltzmann code are compared with Peterson and Allen's CSDA and Bretagne *et al.*'s approach (which neglected electron-atom and Coulomb collisions). These differences are particularly prominent for the 4s configuration. The power loss in excitation of the 4s levels, calculated with our Boltzmann code, is 16%, while Peterson and Allen report only 6% and Bretagne *et al.* - 9%. Peterson and Allen consider only excitation to both resonance states neglecting excitations to the metastable states (or, rather, adding the latter to the composite forbidden transitions), which may explain their lower value compared to Bretagne *et al.* The difference between the present calculations and Bretagne *et al.* results are due to the phenomena described in the former paragraph, namely, the Maxwellization of the EEDF and the presence of more electrons beyond the excitation threshold of Ar compared

to CSDA. The results for the 4p configuration are in closer agreement: our calculations show a power deposition of 6.4%, Peterson and Allen report 5% and Bretagne *et al.* - 4%. The power deposition to the 3d configuration is the same as Peterson and Allen. Obviously, the largest differences in the power deposition occur for the lowest lying levels, where the effect of maxwelization of the EEDF is most prominent. For levels close to the continuum the difference between the simulated CSDA and the solution of the electron Boltzmann equation is gradually reduced. Thus our results demonstrate that the solution of the electron Boltzmann equation is more accurate than the CSDA. The comparison also demonstrates the importance of the elastic electron-electron collisions. If neglected, the EEDF resembles the electron energy degradation spectra of the CSDA. This is the case with the approach used by Bretagne *et al.* Even though they use a Boltzmann code, the EEDF is fairly consistent with the distribution function calculated with the CSDA, due to the lack of elastic collisions.

The individual contributions to the ionization terms of Eq. (3) in the particle balance Eq. (2) for pure Ar can be compared with that of Peterson and Allen. We found that $R_{Ar,L}^{ion}/R_{Ar,M}^{ion} = 0.019$, while Peterson and Allen's value is 0.0046. The sole reason for this difference lies in the adopted cross section for inner shell ionization: the cross section used in this work is approximately four time larger compared to Peterson and Allen's cross section. This explains the four times larger ratio of inner to valence shell ionization rate we calculate as compared to Peterson and Allen. In either case the contribution of the inner shell ionization in the particle balance is negligible, but the fundamental role the inner shell ionization plays is not limited to that. It affects the energy per ion-electron pair, which is one of the most important characteristics of any e-beam sustained plasma, and matching experimentally observed values is one of our primary objectives. According to its definition, the energy per ion-electron pair is a result of an interplay between power loss and ionization rate. As already mentioned, Peterson and Allen's ionization rate increases only by about 0.5% due to inner shell ionization. The power loss, however, increases by about 7.5% and Peterson and Allen calculate an energy per ion-electron pair of $\mathcal{W}_{ei} = 29$ eV; larger then the reported 26 eV. Peterson and Allen made only a guess for the inner shell ionization cross

section, which is too small. Even though they underestimated the role of the inner shell ionization, their value for the energy per ion-electron pair is larger than the experimental value. For the improved cross sections the power loss due to inner shell ionization becomes $\sim 30\%$ of the beam power, which, in the absence of other processes, gives an \mathcal{W}_{ei} above 30 eV. The solution must incorporate Auger ionization, which further enhances the ionization rate and heats the electrons, an effect, opposite to the inner shell ionization. With the Auger ionization accounted for, the energy per ion-electron pair for pure Ar calculated in this work is 25 eV, in close agreement with data (26.2 eV). Bretagne *et al.* computed ~ 26 eV for the energy per ion-electron pair, but did not take into account the inner shell ionization. Neither Peterson and Allen nor Bretagne *et al.* considered Auger ionization. The analysis clearly shows that both the inner shell and Auger ionizations must be taken into account.

A comparison with Peterson and Allen and Bretagne *et al.* can help outline another difference. As mentioned in the Introduction, Peterson and Allen calculated excitation-to-ionization ratio $\eta_{Ar}^{exc} \approx 0.28$. Bretagne *et al.* got a slightly higher value, $\eta_{Ar}^{exc} \approx 0.35$. These two values are close because, as explained above, the approaches used in both articles are almost identical. Our excitation-to-ionization ratio at negligible degree of ionization is $\eta_{Ar}^{exc} \approx 0.38$, very close to that reported by Bretagne *et al.* But at degree of ionization (4×10^{-5}) (typical for most e-beam deposition plasmas), we calculated $\eta_{Ar}^{exc} \approx 0.61$, which is twice higher compared to both Peterson and Allen and Bretagne *et al.* The reason for such a high value is again the impact of the Coulomb collisions between electrons on the EEDF.

V. SUMMARY

Electron impact ionization and excitation resulting from e-beam deposition has been evaluated using the electron energy distribution function calculated from the steady state, spatially independent, electron Boltzmann equation. The chosen target gas is appropriate to a KrF* laser amplifier: 68.5% Ar, 31% Kr, and 0.5% F₂ at atmospheric density. The beam energy was varied from 1 to 650 keV and the beam power density from 1 to 1000 kW/cm³.

Interactions of the beam electrons and all generations of secondaries were followed down to an energy of 0.01 eV. The degradation processes included 12 excitations channels from ground state Ar (Fig. 1) and likewise for Kr (Fig. 3). The valence and inner shell ionizations for both Ar and Kr were treated with energy differential cross sections. The low energy component of the distribution function, i.e., below the first excitation thresholds of Ar and Kr, was subject to F₂ vibrational excitation, electronic excitation, molecular dissociation, and attachment (Fig. 5). Valence shell ionization of F₂ was also treated. The electron density and the mean energy of the bulk electrons were calculated self-consistently since electron attachment with F₂ is the dominant electron loss process. Coulomb collisions between electrons act to Maxwellianize the distribution function as the electron density increases with P_{beam} (Fig. 7).

The assumption of the present Boltzmann model is that electron collisions with the ground state species of Ar, Kr, and F₂ are primarily responsible for shape of the EEDF. Though interactions of the beam and secondary electrons with excited state species and other rare gas molecules occur, the density of the these latter species is about four orders of magnitude smaller than ground state Ar and Kr. The contributions to ionization by electron collisions with excited species is about 10%. For instance, at $P_{beam}=300$ kW/cm³, Fig. 8 indicates $n_e=4\times 10^{14}$ cm⁻³ and an average bulk electron energy of 2.7 eV. Using the ionization rate coefficients for Ar* and Kr* from Ref.⁹ and an excited state density of 10¹⁵ cm⁻³, we find an ion production rate from excited states of $\sim 5\times 10^{21}$ cm⁻³s⁻¹. The rate from the beam is $P_{beam}/\mathcal{W}_{ei}\sim 8\times 10^{22}$ cm⁻³s⁻¹.

One objective of the research was to match both the data for the energy per ion-electron pair as well as the stopping power results from Berger and Seltzer. This was accomplished by addressing two aspects of inner shell ionization. The first is Auger emission following each inner shell ionization event. Though the latter process does not add significantly to the total ionization rate, it leads to a value for \mathcal{W}_{ei} in pure Ar of over 30 eV due to the large energy loss. The inclusion of Auger emission returns the lost energy as an energetic electron which produces further ionization. The resulting value of \mathcal{W}_{ei} for Ar is 25.0 eV, close to

the experimental data of 26.2 eV. In pure Kr we find $\mathcal{W}_{ei} = 23.9$ eV while the data is 24.2 eV. For the KrF* mixture the energy per ion-electron pair is calculated as 24.6 eV. In all cases $\mathcal{W}_{ei} = P_{beam}/R_{tot}^{ion}$ is found to be independent of the beam power density and energy even though the distribution function \tilde{f} does change with these parameters. The sublinear increase in the electron density with beam power (Fig. 8) coupled with the slight increase in \tilde{f} (Fig. 7) leads to an ionization rate R_{tot}^{ion} which is proportional to P_{beam} . The second aspect is the width of the energy differential cross section for inner shell ionization. In the absence of L-shell ionization, the calculated loss function of Ar is a factor of two below the value of Berger and Seltzer at 10 keV. When the width is set at 2/3 of the Ar L-shell ionization potential, as is the case from experiments on M-shell ionization, then the loss function agrees with the stopping power Fig. 6a. A similar procedure for Kr shows some improvement, but not as dramatic and may indicate the need to consider not only the inner M-shell but also the L-shell ionization.

A second objective was the detailed treatment of the excitation efficiencies for Kr by an e-beam in a realistic KrF* mixture. This has not been studied before. The Boltzmann solution indicates that the EEDF is sensitive to the beam power density due to electron Coulomb collisions coupled with the increase in electron density as P_{beam} rises. It accounts for the relaxation of the distribution function near the lowest excitation thresholds of Ar and Kr and influences the excitation efficiency. Such an effect cannot be treated by either the CSDA nor a reduced Boltzmann model. At low beam power density the summed excitation-to-ionization ratio is 0.38 for Ar and rises to 0.41 as P_{beam} increases to 1 MW/cm³ (Fig. 11). Over the same range of P_{beam} , the calculated ratio for Kr increases from 0.54 to 0.8. The excitation ratio for Kr is significantly larger than the values used in existing kinetic models for e-beam driven KrF* amplifiers.

The increase of the beam excitation rate as concluded here can have several effects upon models for the KrF kinetics in an amplifier. First, there is an increase in the KrF* pumping rate through the harpoon reaction $Kr^* + F_2$ and $KrF^* + F$. Also excited Ar undergoes a similar harpoon reaction to form ArF* and the latter species leads to KrF* through the

displacement reaction: $\text{ArF}^* + \text{Kr}$ and $\text{KrF}^* + \text{Ar}$. Second, the enhanced beam formation rate of excited states increases the absorption of the lasing photons. A. Mandl, *et al.*⁸ found that the photo-absorption of Ar and Kr excited states was nearly equal to that of the dominant absorber, F^- . Their model is based on an excitation-to-ionization ratio of only 0.3, significantly less than what has been calculated here. Third, the two harpoon reactions mentioned above contribute to the depletion of F_2 , though this is of secondary importance compared to dissociative attachment of F_2 . Inclusion of the enhanced excitation-to-ionization ratio in a KrF kinetics model would likely require adjustment to other reaction rates in order to reproduce agreement with experiments as found with kinetic models using lower excitation-to-ionization ratios.

ACKNOWLEDGMENTS

We wish to thank John Sethian and Steve Obenschain of the Laser Physics Branch at NRL, Steve Swanekamp of JAYCOR, Stu Searles of RSI and Paul Kepple of the Plasma Physics Branch for many fruitful discussions related to e-beam deposition. This work was supported by the US Department of Energy, Defense Programs.

REFERENCES

- ¹ L.A. Rosocha and K.B. Riepe, *Fusion Technology* **11**, 576 (1987).
- ² J.D. Sethian, C.J. Pawley, S.P. Obenschain, K.A. Gerber, V. Serlin, C.A. Sullivan, T. Lehecka, W.D. Webster, M.W. McGeoch, I.D. Smith, P.A. Corcoran, and R.A. Altes, *IEEE Trans. Plasma Sci.* **25**, 221 (1997).
- ³ J.D. Sethian, S.P. Obenschain, K.A. Gerber, C.J. Pawley, V. Serlin, C.A. Sullivan, W.D. Webster, A.V. Deniz, T. Lehecka, M.W. McGeoch, R.A. Altes, P.A. Corcoran, I.D. Smith, and O.C. Barr, *Rev. Sci. Instrum.* **68**, 2357 (1997).
- ⁴ J.D. Sethian, M. Meyers, I.D. Smith, V. Carboni, J. Kishi, D. Morton, J. Pearce, B. Bowen, L. Schlitt, O. Barr, and W. Webster *IEEE Trans. Plasma Sci.* **28**, 1333 (2000).
- ⁵ A. Suda, M. Obara, and A. Noguchi, *Fusion Technology* **11**, 548 (1987).
- ⁶ M.W. McGeoch, P.A. Corcoran, R.G. Altes, I.D. Smith, S.E. Bodner, R.H. Lehmberg, S.P. Obenschain, and J.D. Sethian, *Fusion Technology* **32**, 610 (1997).
- ⁷ W.L. Morgan and A. Szöke, *Phys. Rev. A* **23**, 1256 (1981).
- ⁸ A. Mandl, D. Klimek, and J.H. Parks, *J. Appl. Phys.* **55**, 3940 (1984).
- ⁹ F. Kannari, M. Obara, and T. Fujioka, *J. Appl. Phys.* **57**, 4309 (1985).
- ¹⁰ S.J. Czuchlewski, D.E. Hanson, B.J. Krohn, and A.R. Larson, *Fusion Technology* **11**, 560 (1987).
- ¹¹ M.W. McGeoch, in *Naval Research Laboratory, Report No. NRL/PU/6730-94-264*, 1994 (unpublished).
- ¹² G.N. Whyte, *Radiation Res.* **18**, 265 (1963).
- ¹³ L.G. Christophorou, *Atomic and Molecular Radiation Physics* (Wiley-Interscience, London, 1971), p.35.

- ¹⁴ L.R. Peterson and J.E. Allen, Jr., J. Chem. Phys. **56**, 6068 (1972).
- ¹⁵ L.R. Peterson, Phys. Rev. **187**, 105 (1969).
- ¹⁶ L.R. Peterson, T. Sawada, J.N. Bass, and A.E.S. Green, Comp. Phys. Comm. **5**, 239 (1973)
- ¹⁷ M.J. Berger and S.M. Seltzer, "Tables of Losses and Ranges of Electrons and Positrons," NASA Report No. SP-3012, 1964 (unpublished).
- ¹⁸ D.C. Lorents, Physica **82C**, 19 (1976).
- ¹⁹ J. Bretagne, G. Delouya, J. Godart, and V. Puech, J. Phys. D: Appl. Phys. **14**, 1225 (1981).
- ²⁰ A.E.S. Green and T. Sawada, J. Atmospheric and Terrestrial Phys. **34**, 1719 (1972)
- ²¹ D.A. Vroom, R.L. Palmer, and J.Wm. Mc Gowan, J. Chem. Phys. **66**, 647 (1977).
- ²² H.C. Straub, P. Renault, B.G. Lindsay, K.A. Smith, and R.F. Stebbings, Phys. Rev. A **52**, 1115 (1995).
- ²³ Dayayshankar, Physica **111C**, 134, (1981).
- ²⁴ Dayayshankar, M.A. Prasad, and K. Unnikrishnan, Physics Lett. **90A**, 402, (1982).
- ²⁵ C.J. Elliott and A.E. Greene, J. Appl. Phys. **47**, 2946 (1976).
- ²⁶ J.E. Chilton, J.B. Boffard, R.S. Schappe. and C.C. Lin, Phys. Rev. A **57**, 267 (1998).
- ²⁷ J.E. Chilton, M.D. Stewart, Jr., C.C. Lin, Phys. Rev. A **62**, 032714-1 (2000).
- ²⁸ A. Dasgupta, M. Blaha, and J.L. Giuliani, Phys. Rev. A **61**, 012703-1 (1999).
- ²⁹ D.R. Suhre and J.T. Verdeyen, J. Appl. Phys. **47(10)**, 4484 (1976).
- ³⁰ J.W. Keto, J. Chem Phys. **74**, 4445 (1981).
- ³¹ F. Kannari and W.D. Kimura, J. Appl. Phys. **64**, 500 (1988).

- ³² S.P. Slinker, R.D. Taylor, and A.W. Ali, J. Appl. Phys. **63**, 1 (1988).
- ³³ S.P. Slinker, A.W. Ali, and R.D. Taylor, J. Appl. Phys. **67**, 679 (1990).
- ³⁴ S.C. Soong, Radiation Research **67**, 187 (1976).
- ³⁵ D. Loffhagen and R. Winkler, J. Comp. Phys. **112**, 91 (1994).
- ³⁶ D. Uhrlandt, M. Schmidt, and R. Winkler, Comp. Phys. Comm. **118**, 185 (1999).
- ³⁷ E. Eggarter, J. Chem. Phys. **62**(3), 833 (1975).
- ³⁸ G. M. Petrov and C.M. Ferreira, "A Collisional-Radiative Model for Argon Discharges at Intermediate and High Pressures", Internal Report CFP 10/97, Instituto Superior Tcnico, Lisbon Technical University, Portugal.
- ³⁹ A. Bogaerts, R. Gijbels, and J. Vlcek, J. Appl. Phys. **84**(1), 121 (1998).
- ⁴⁰ M. Hayashi, private communication.
- ⁴¹ K. Tachibana, Phys. Rev. A **34**, 1007 (1986).
- ⁴² R.S. Schappe, M.B. Schulman, L.W. Anderson, and C. C. Lin, Phys. Rev. A **50**, 444 (1994).
- ⁴³ N.T. Padial, G.D. Meneses, F.J. da Paixão, and Gy. Csanak, Phys. Rev. A **23**, 2194 (1981).
- ⁴⁴ A. Chutjian and D.C. Cartwright, Phys. Rev. A **23**, 2178 (1981).
- ⁴⁵ D.H. Madison, C.M. Maloney and J.B. Wang, J. Phys. B: At. Mol. Opt. Phys. **31**, 873 (1998).
- ⁴⁶ J.K. Ballou, C.C. Lin, and F.E. Fajen, Phys. Rev. A **8**, 1797 (1973).
- ⁴⁷ I.P. Bogdanova, V.D. Marusin, and V.E. Yakhontova, Opt. Spectrosk. (USSR) **44**(4), 368 (1978).

- ⁴⁸ J.E. Chilton and C.C. Lin, Phys. Rev. A **60**, 3712 (1999).
- ⁴⁹ H.W. Drawin, Z. Physik **225**, 483 (1969).
- ⁵⁰ I.I. Sobelman, L.A. Vainstein and E.A. Yukov, "Excitation of atoms and broadening of spectral lines", Springer-Verlag, Berlin, 206 (1981).
- ⁵¹ C.M. Lee and K.T. Lu, Phys. Rev. A **8**, 1241 (1973).
- ⁵² S.K. Srivastava, H. Tanaka, A. Chutjian, and S. Trajmar, Phys. Rev. A **23**, 2156 (1981).
- ⁵³ C.B. Opal, E.C. Beaty, and W.K. Peterson, At. Data **4**, 209 (1972).
- ⁵⁴ D. Rapp and P. Englander-Golden, J. Chem. Phys. **43**, 1464 (1965).
- ⁵⁵ R.S. Freund, R.C. Wetzel, R.J. Shul, and T.R. Hayes, Phys. Rev. A **41**, 3575 (1990).
- ⁵⁶ E.J. McGuire, Phys. Rev. A **16**, 73 (1977).
- ⁵⁷ H. Date, Y. Sakai and H. Tagashira, J. Phys. D: Appl. Phys. **22**, 1478 (1989).
- ⁵⁸ S. Trajmar, S.K. Srivastava, H. Tanaka, and H. Nishimura, Phys. Rev. A **23**, 2167 (1981).
- ⁵⁹ G.D. Meneses, F.J. da Paixão, and N. T. Padial, Phys. Rev. A **32**, 156 (1985).
- ⁶⁰ I.P. Bogdanova and S.V. Yurgenson, Opt. Spectrosk. (USSR) **62(3)**, 428 (1987).
- ⁶¹ S. Kaur, S. Srivastava, R.P. McEachran, and A.D. Stauffer, J. Phys. B: At. Molec. Phys. **31**, 4833 (1988).
- ⁶² A. Dasgupta, K. Bartschat, D. Vaid, A.N. Gram-Grzhimailo, D.H. Madison, M. Blaha, and J.L. Giuliani, to be submitted to Phys. Rev. A (2001).
- ⁶³ A. Delâge and J-D Carette, J. Phys. B: Atom. Molec. Phys. **9**, 2399 (1976)
- ⁶⁴ M. Hayashi and T. Nimura, J. Appl. Phys. **54(9)**, 4879 (1983).
- ⁶⁵ W.L. Morgan, Plasma Chem. Plasma Proc. **12(4)**, 449 (1992)

FIGURES

FIG. 1. Excitation cross sections of Ar for allowed (a) and forbidden (b) transitions.

FIG. 2. Total excitation, momentum transfer, inner and valence shell ionization cross sections for Ar.

FIG. 3. Excitation cross sections of Kr for allowed (a) and forbidden (b) transitions.

FIG. 4. Total excitation, momentum transfer, inner and valence shell ionization cross sections for Kr.

FIG. 5. Momentum transfer, attachment, vibrational excitation, electronic excitation, dissociation and ionization cross sections of F_2 .

FIG. 6. (a) Loss function of Ar calculated without inner shell ionization (A) and with inner shell ionization having an energy width $\Gamma=40$ eV (B) and 160 eV (B'). For comparison, the electron stopping power from Berger and Seltzer is also plotted. (b) Similar calculation for Kr using an energy width of $\Gamma=40$ eV (B) and 60 eV (B').

FIG. 7. EEDF at beam power varying from 1 kW/cm³ to 1 MW/cm³ for $p_{Ar}=562.5$ Torr, $p_{Kr}=254.4$ Torr, $p_{F_2}=3.9$ Torr and $U_{beam}=650$ keV.

FIG. 8. Electron density (a) and mean energy of the bulk electrons (b) versus beam power. The discharge parameters are the same as in Fig. 7.

FIG. 9. Fractional power loss in collisions with Ar (a), Kr (b) and F_2 (c). The discharge parameters are the same as in Fig. 7.

FIG. 10. Branching ratios for energy deposition on individual Ar (a) and Kr (b) excited states. The discharge parameters are the same as in Fig. 7.

FIG. 11. Total excitation-to-ionization ratios for Ar and Kr. The discharge parameters are the same as in Fig. 7.

FIG. 12. EEDF at beam energy of 1 KeV, 10 KeV, 100 Kev and 650 KeV for $p_{Ar}=562.5$ Torr, $p_{Kr}=254.4$ Torr, $p_{F_2}=3.9$ Torr and $P_{beam}=346$ kW/cm³.

FIG. 13. EEDF in Ar at degree of ionization 4×10^{-5} (full line) and zero (dashed line).

TABLES

TABLE I. Ar electron impact excitation cross sections from the ground state, $x = u/\Delta E$.

final state	$\sigma(cm^{-2})$	ΔE (eV)	f	ref
Ar($4s[3/2]_2$)	$4.0 \times 10^{-16}(x^2 - 1)(x^6 + 50)^{-1}$	11.548		28
Ar($4s[3/2]_1$)	$7.0 \times 10^{-18}(x - 1)(\ln(1.25x) + 5)x^{-2}$	11.624		28
Ar($4s'[1/2]_0$)	$6.5 \times 10^{-17}(x^2 - 1)(x^6 + 40)^{-1}$	11.723		28
Ar($4s'[1/2]_1$)	$8.9 \times 10^{-17}(x - 1)\ln(1.25x)x^{-2}$	11.828		28
Ar($4p$) ⁽¹⁾	$1.3 \times 10^{-16}(x - 1)x^{-2}$	12.907		28
Ar($4p$) ⁽²⁾	$1.9 \times 10^{-16}(x^4 - 1)(x^{7.5} + 20)^{-1}$	12.907		28
Ar($3d$)	$6.9 \times 10^{-17}(x - 1)\ln(1.25x)x^{-2}$	13.845	2.03×10^{-1}	49
	$+6.5 \times 10^{-17}(x^2 - 1)(x^{4.2} + 0.2)^{-1}$			48
Ar($5s$)	$1.3 \times 10^{-17}(x - 1)\ln(1.25x)x^{-2}$	14.068	4.04×10^{-2}	49
	$+1.6 \times 10^{-17}(x^2 - 1)(x^{4.5} + 0.7)^{-1}$			48
Ar($5p$)	$0.35\sigma_{Ar(4p)}$	14.164		50
Ar($4d$)	$2.0 \times 10^{-17}(x - 1)\ln(1.25x)x^{-2}$	14.711	6.70×10^{-2}	49
Ar($6s$)	$9.3 \times 10^{-17}(x - 1)\ln(1.25x)x^{-2}$	14.839	3.14×10^{-2}	49
Ar**	$1.4 \times 10^{-17}(x - 1)\ln(1.25x)x^{-2}$	15	4.71×10^{-2}	49

TABLE II. Kr electron impact excitation cross sections from the ground state, $x = u/\Delta E$.

final state	$\sigma(cm^{-2})$	ΔE (eV)	f_{eff}	ref
Kr($5s[3/2]_2$)	$1.8 \times 10^{-16}(x^3 - 1)(x^{6.5} + 35)^{-1}$	9.915		62
Kr($5s[3/2]_1$)	$1.0 \times 10^{-16}(x - 1) \ln(1.25x)x^{-2}$	10.033		62
Kr($5s'[1/2]_0$)	$2.8 \times 10^{-17}(x^3 - 1)(x^{6.8} + 70)^{-1}$	10.563		62
Kr($5s'[1/2]_1$)	$5.3 \times 10^{-17}(x - 1) \ln(1.25x)x^{-2}$	10.644		62
Kr($5p$) ⁽¹⁾	$1.3 \times 10^{-16}(x - 1)x^{-2.3}$	11.303		62
Kr($5p$) ⁽²⁾	$4.0 \times 10^{-16}(x^4 - 1)(x^{7.5} + 30)^{-1}$	11.303		62
Kr($4d$)	$7.2 \times 10^{-17}(x - 1) \ln(1.25x)x^{-2}$	12.04	1.60×10^{-1}	49
Kr($6s$)	$7.7 \times 10^{-17}(x - 1) \ln(1.25x)x^{-2}$	12.35	1.80×10^{-1}	49
Kr($6p$)	$0.25\sigma_{Kr(5p)}$	12.50		50
Kr($5d$)	$5.1 \times 10^{-17}(x - 1) \ln(1.25x)x^{-2}$	12.87	1.30×10^{-1}	49
Kr($7s$)	$4.2 \times 10^{-17}(x - 1) \ln(1.25x)x^{-2}$	13.11	1.10×10^{-1}	49
Kr**	$3.2 \times 10^{-17}(x - 1) \ln(1.25x)x^{-2}$	13.30	8.80×10^{-2}	49

TABLE III. Fractional contribution of ionization terms in the particle balance Eq. (2). The beam power and energy are 346 kW/cm^3 and $U_{beam}=650 \text{ keV}$, respectively

specie	ion	%
Ar	M shell	55.0
Ar	L shell	1.4
Ar	Auger	1.4
Kr	N shell	39.4
Kr	M shell	1.3
Kr	Auger	1.3
F ₂		0.2

TABLE IV. Fractional power loss (in percent) for the electron Boltzmann equation (BE) and the simulated Continuous Slowing Down Approximation (CSDA)

process	BE	CSDA
elastic	5.5	16.3
excitation (total)	30.5	19.6
ionization (valence shell)	60.6	60.7
ionization (inner shell)	3.4	3.4

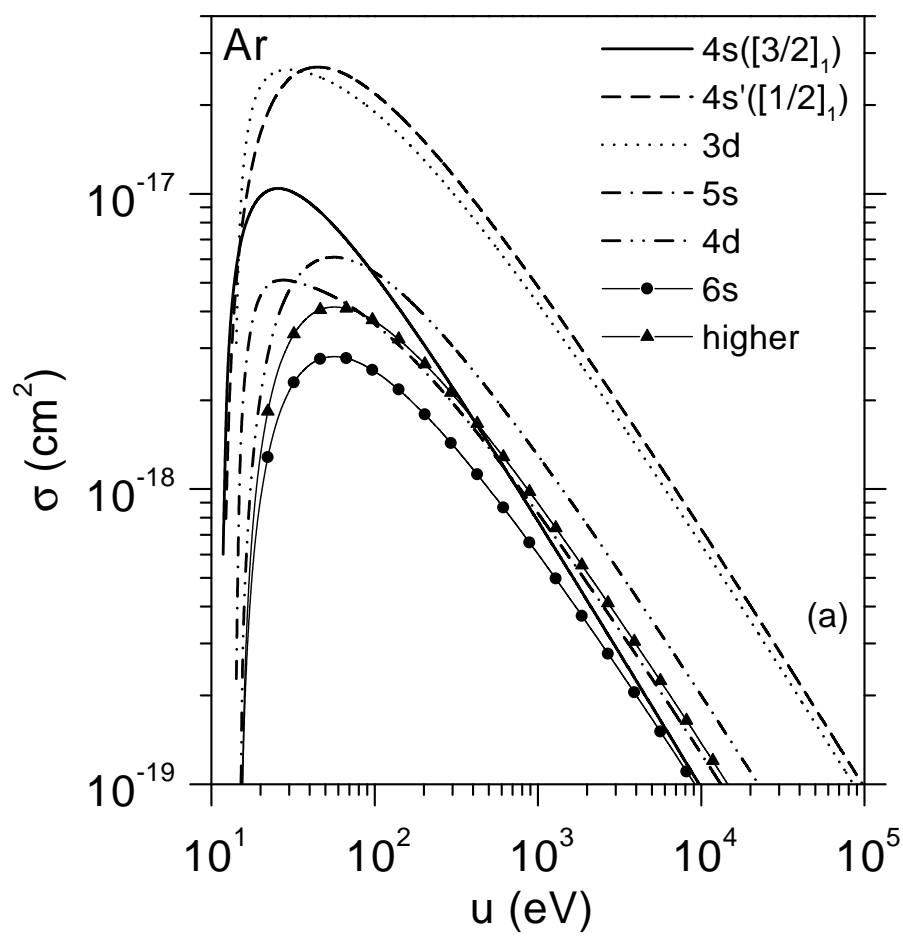


Fig. 1a

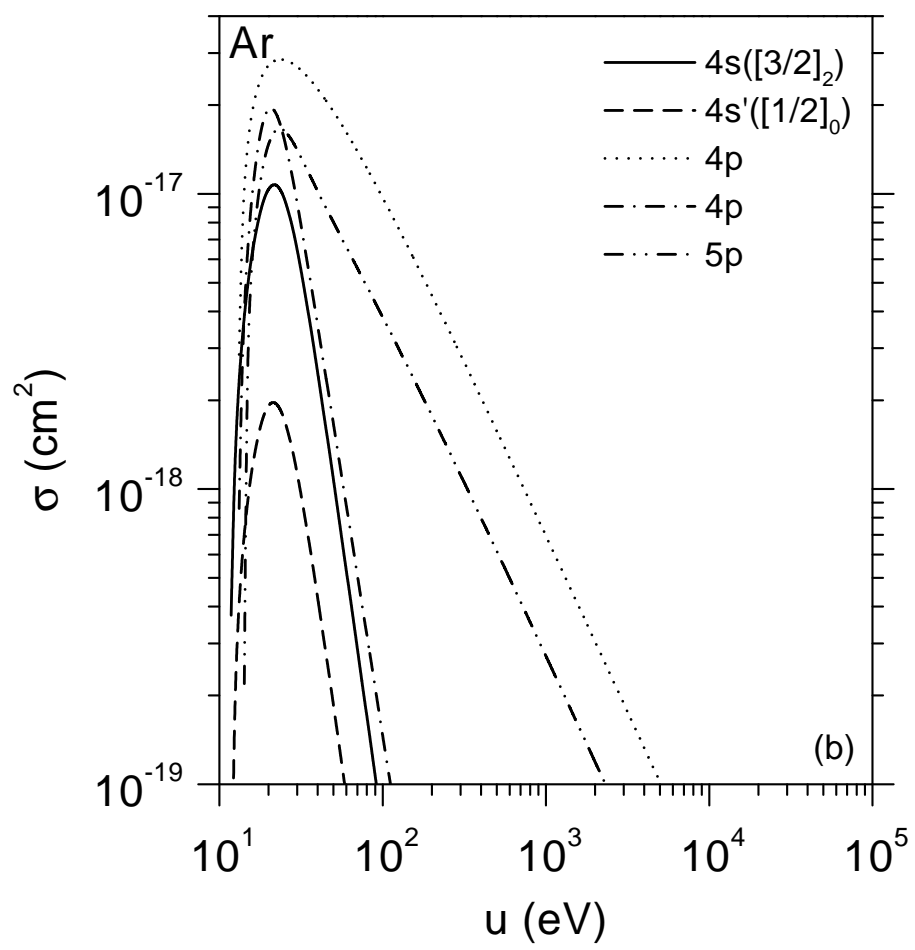


Fig. 1b

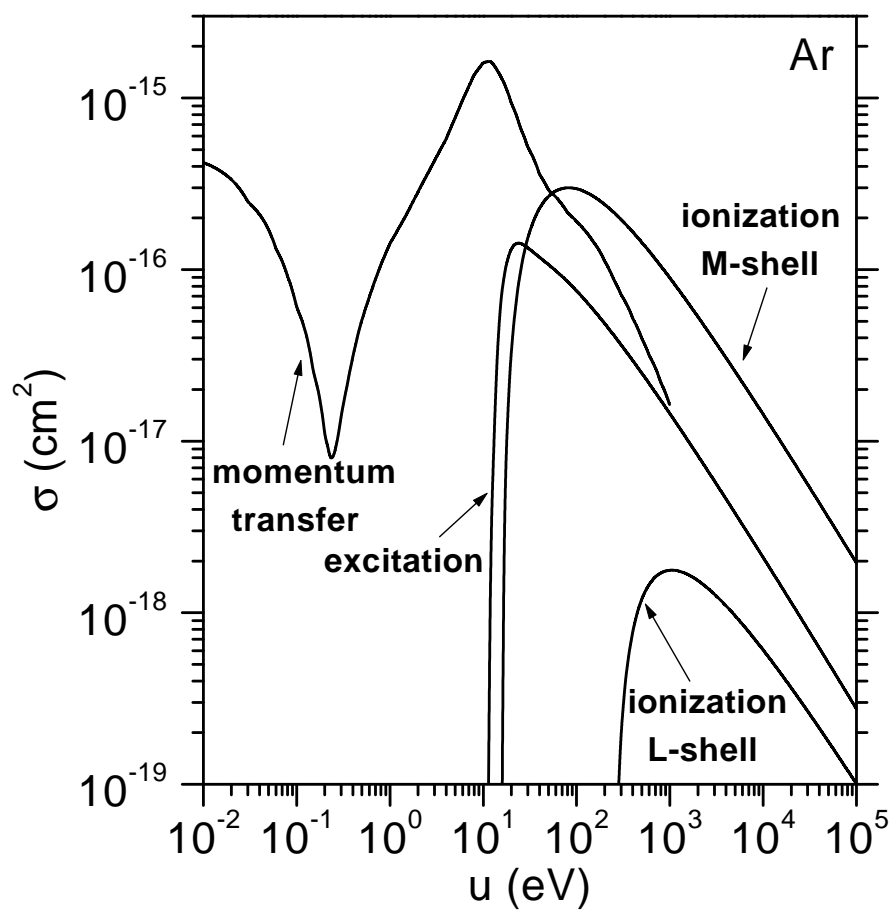


Fig. 2

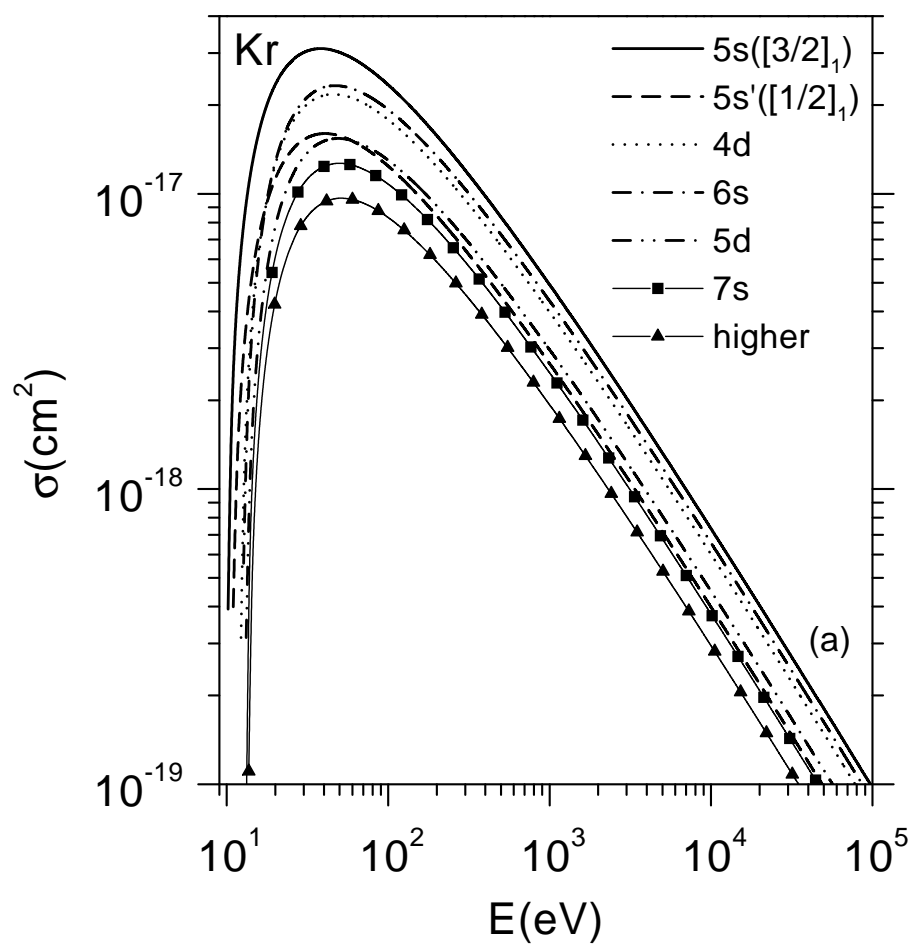


Fig. 3a

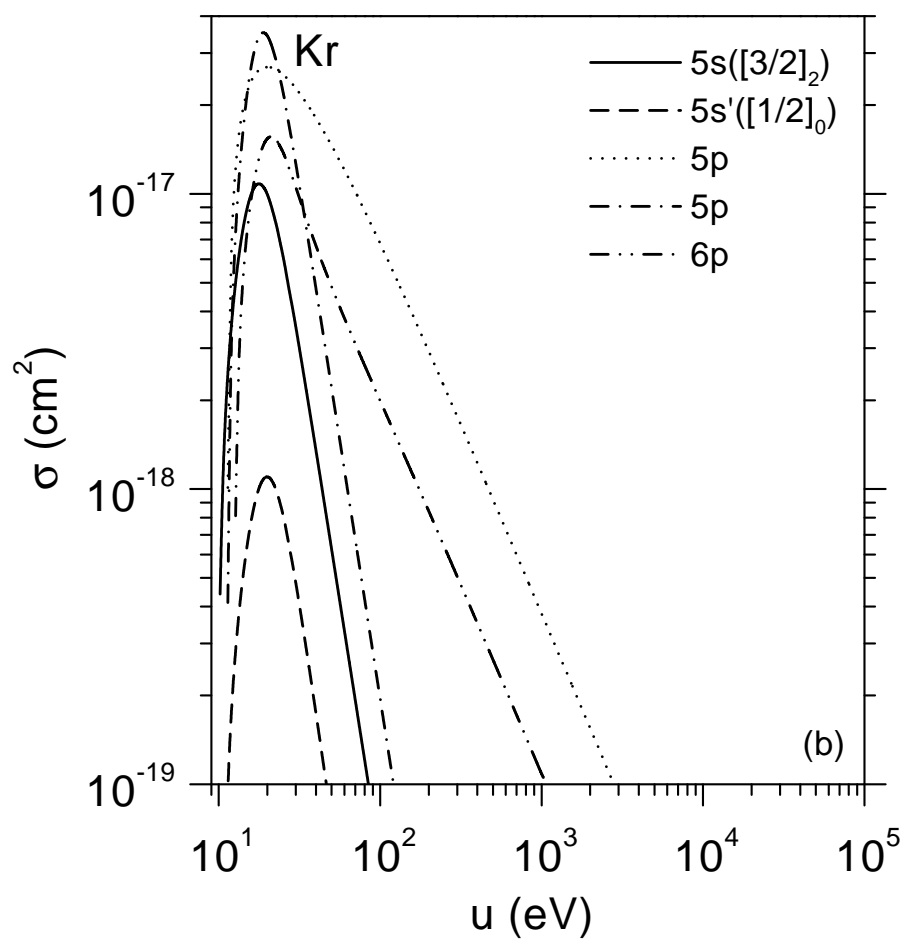


Fig. 3b

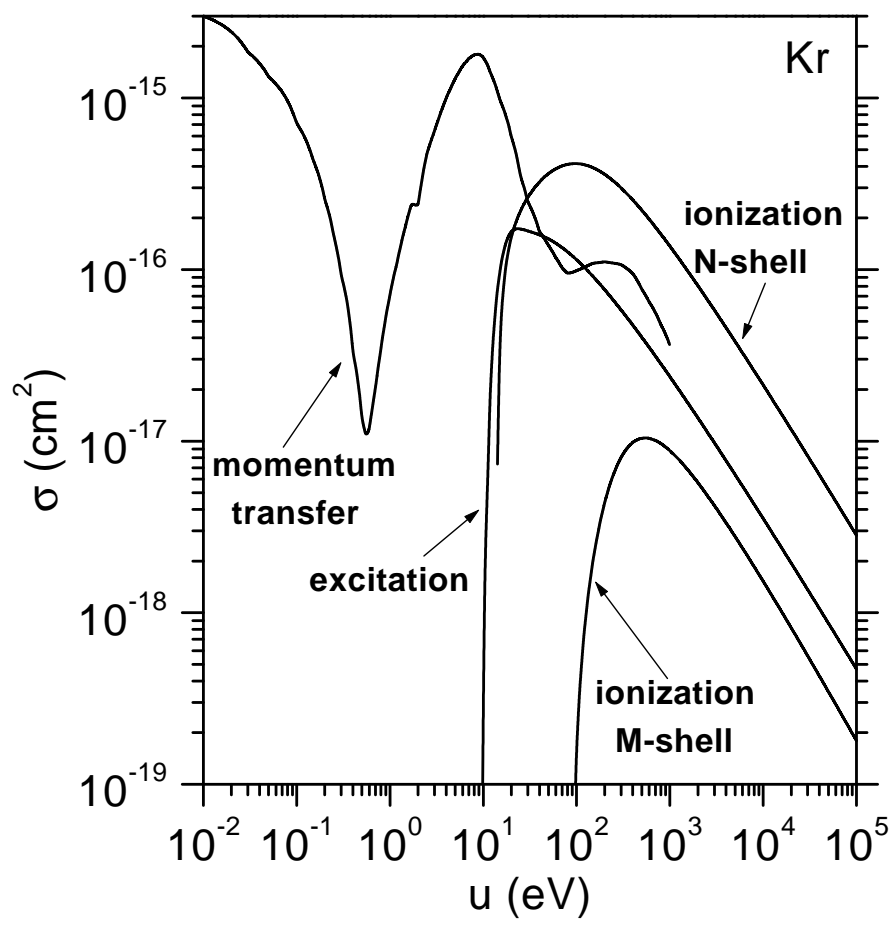


Fig. 4

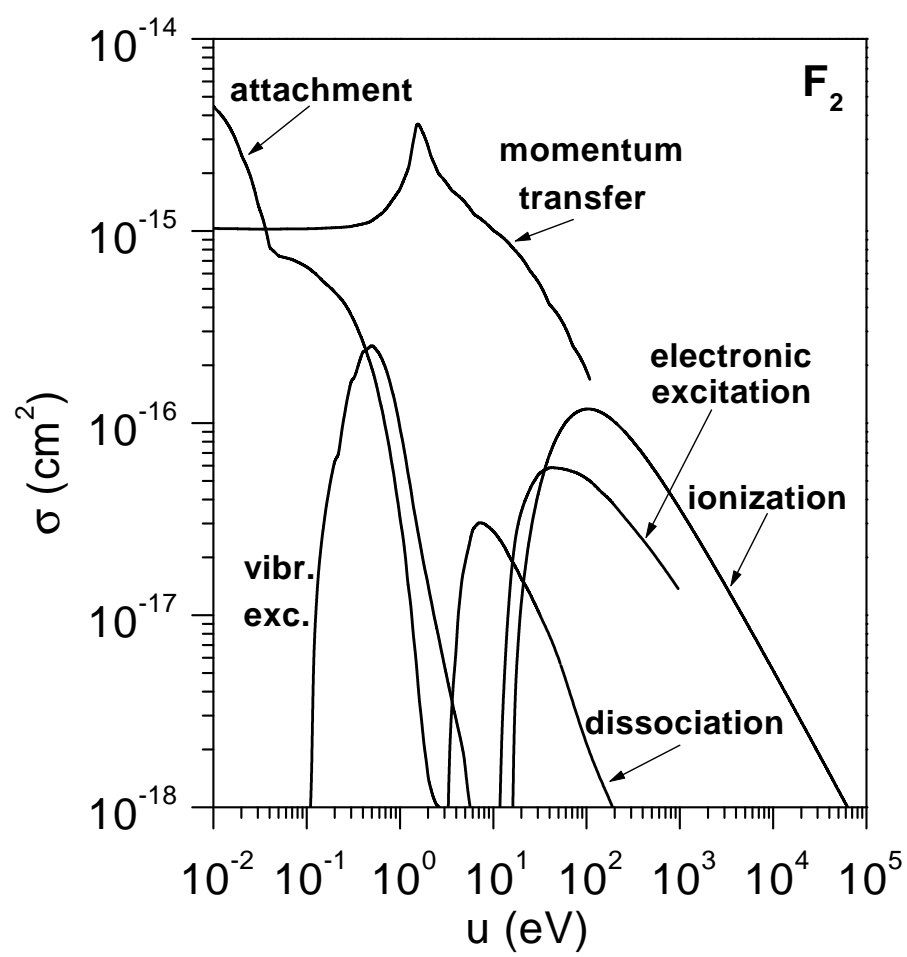


Fig.5

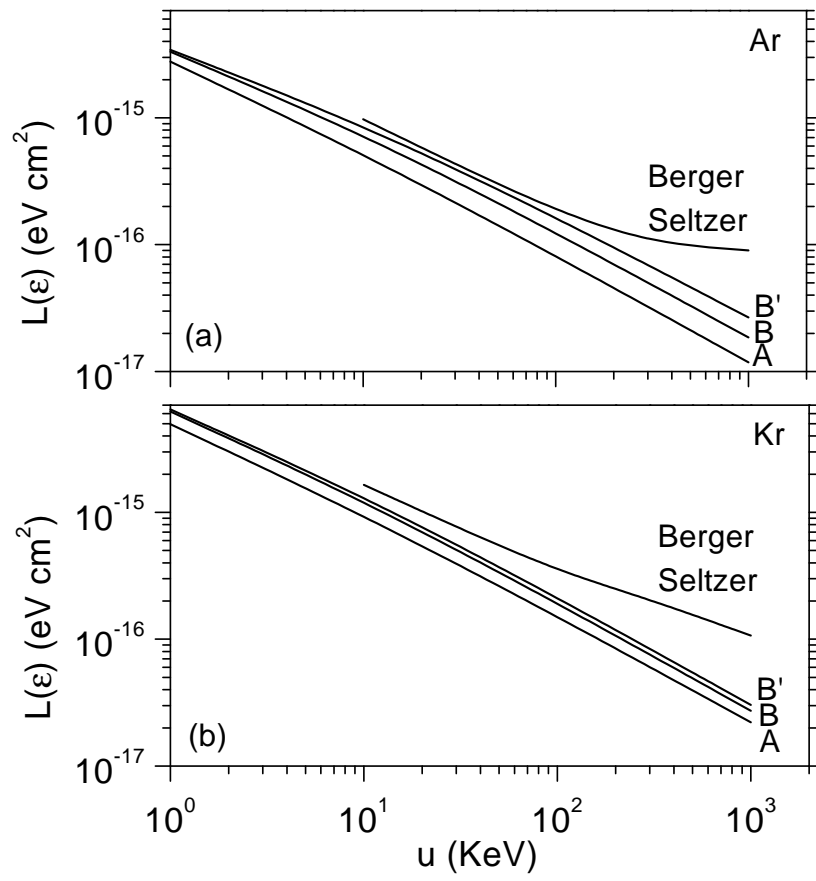


Fig. 6

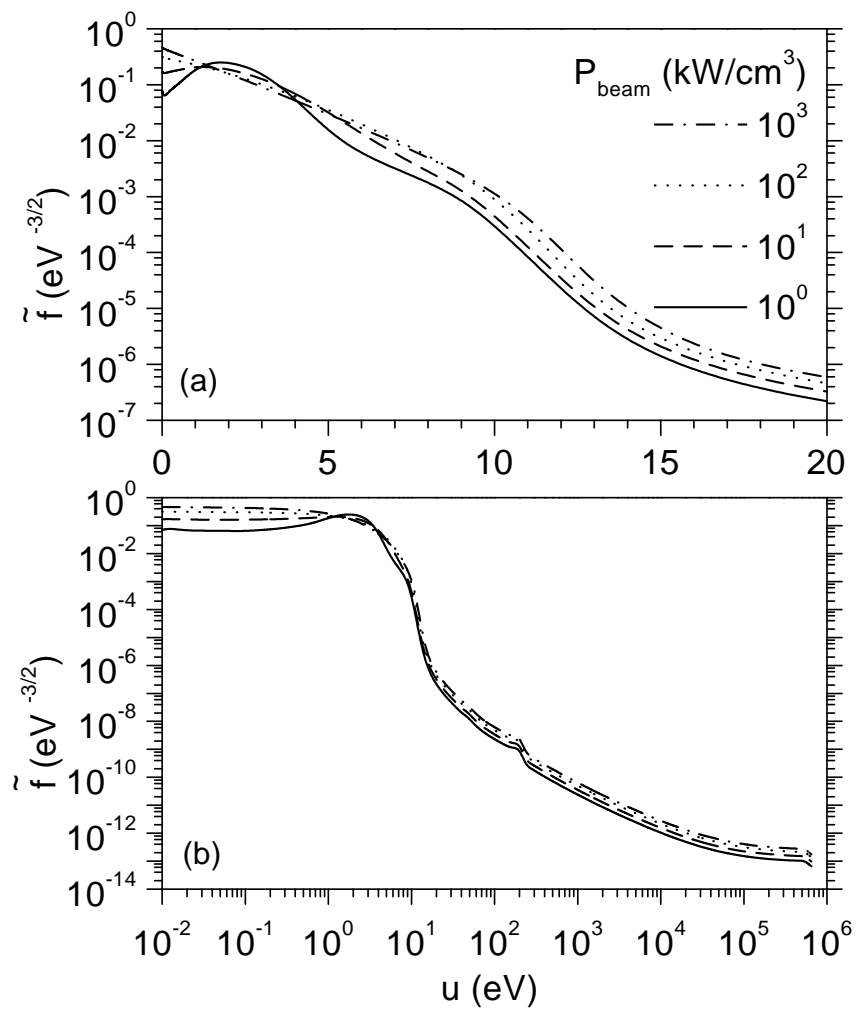


Fig. 7

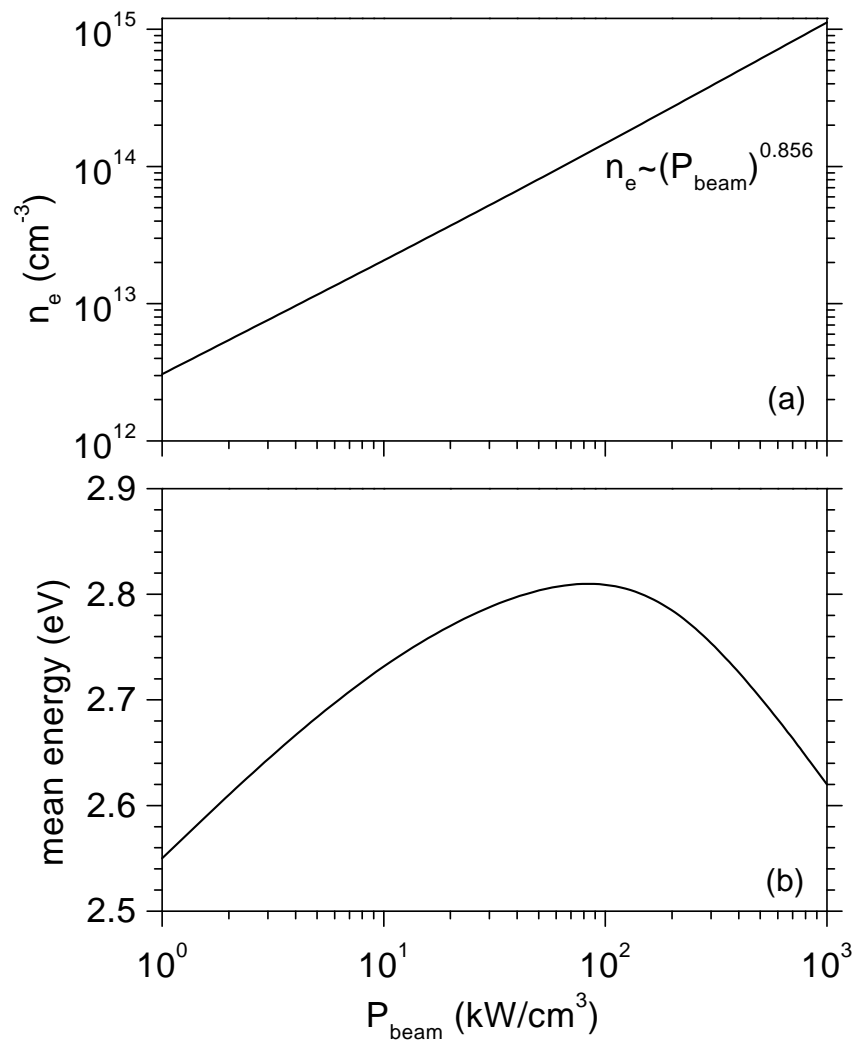


Fig. 8

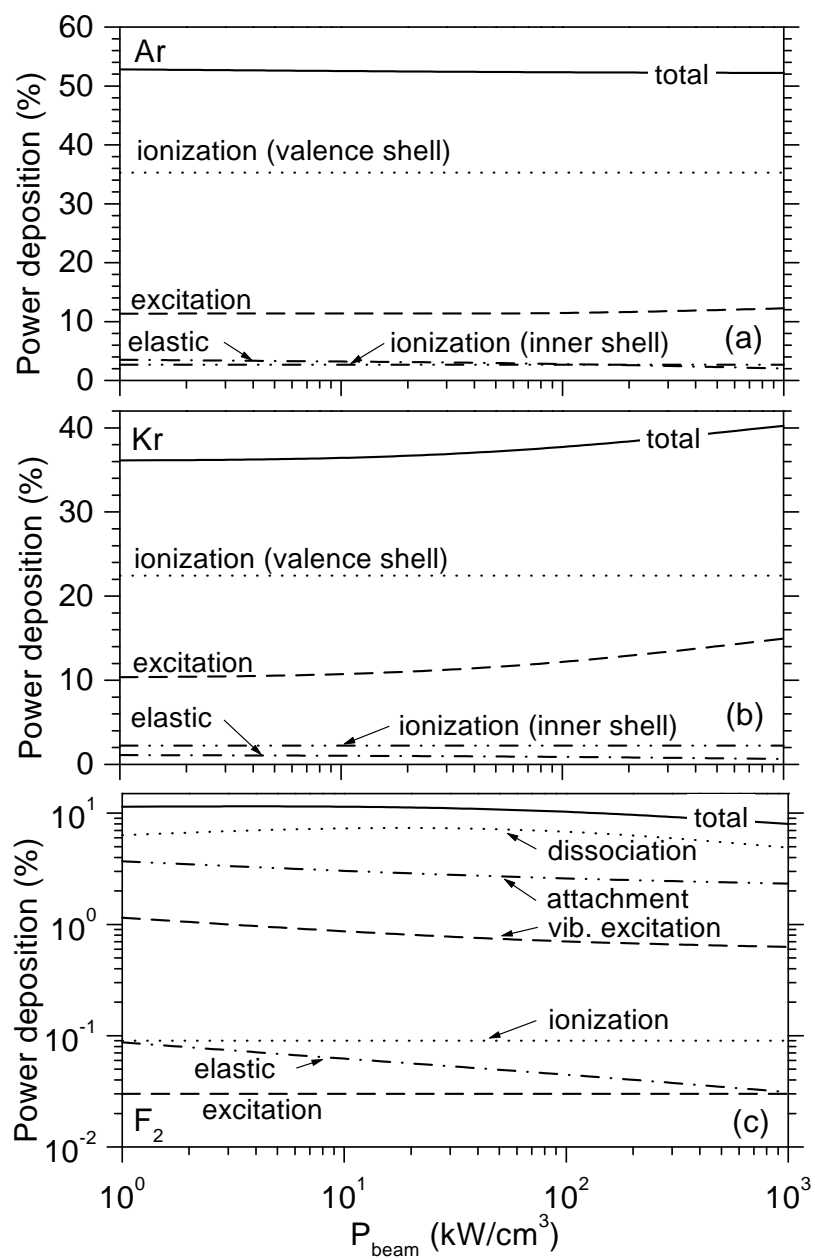


Fig. 9

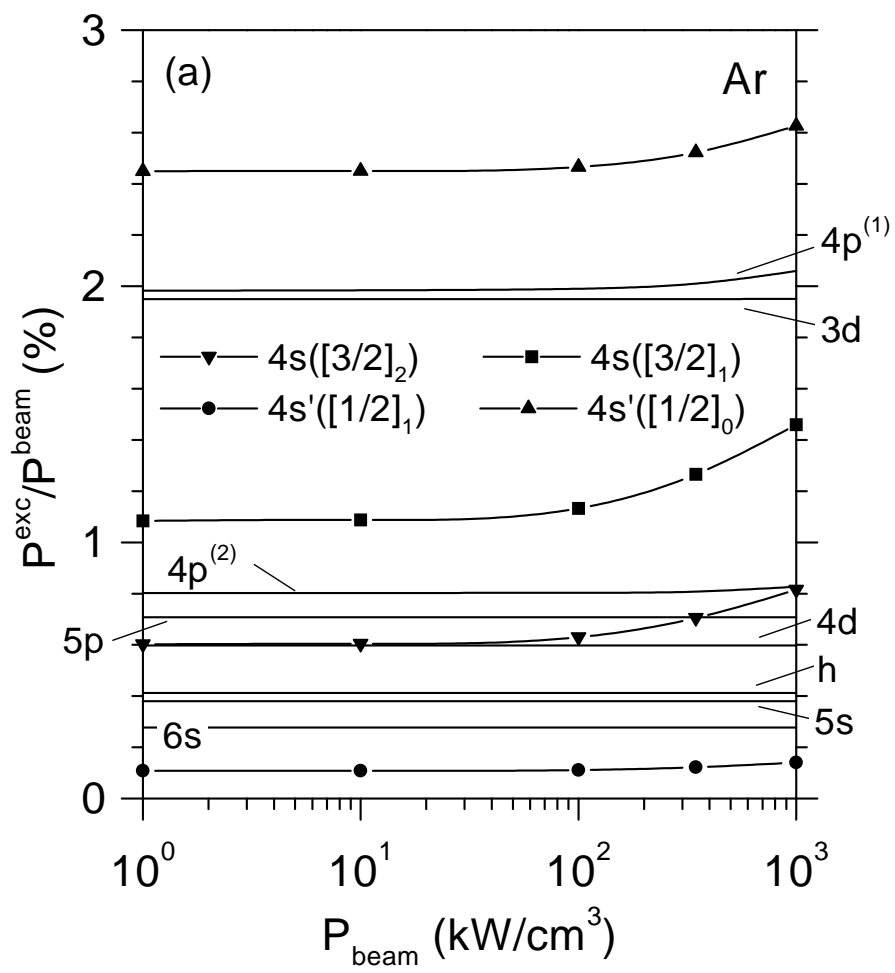


Fig. 10a

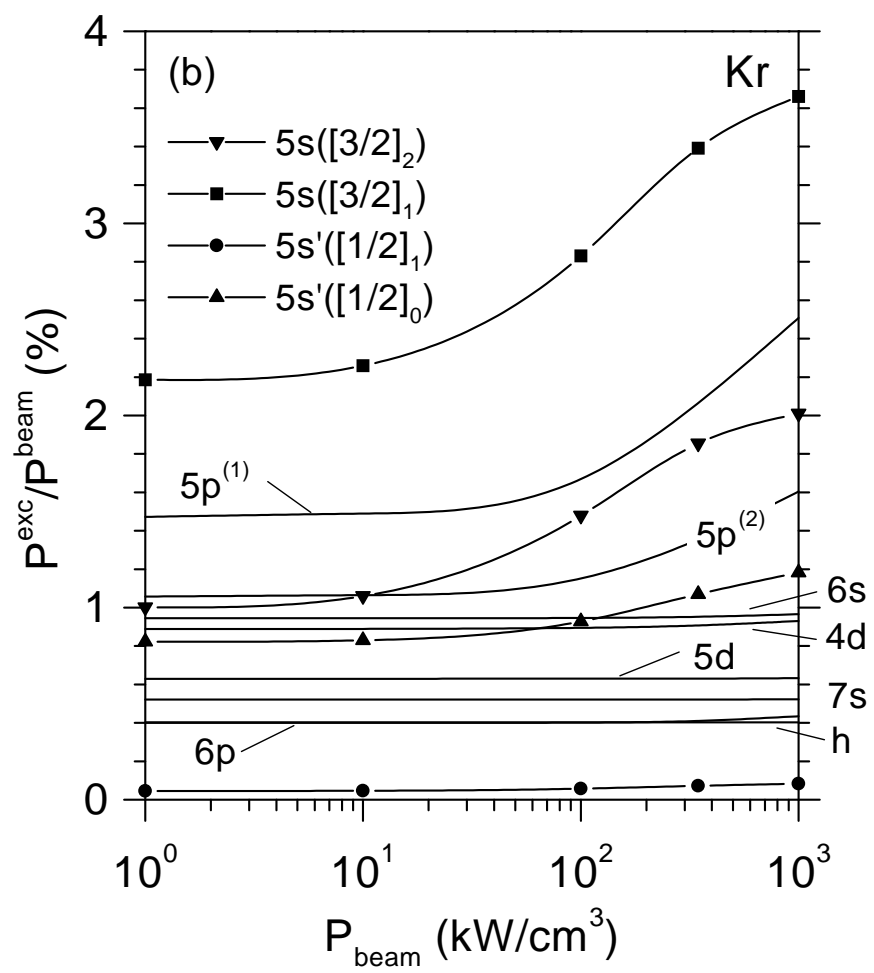


Fig. 10b

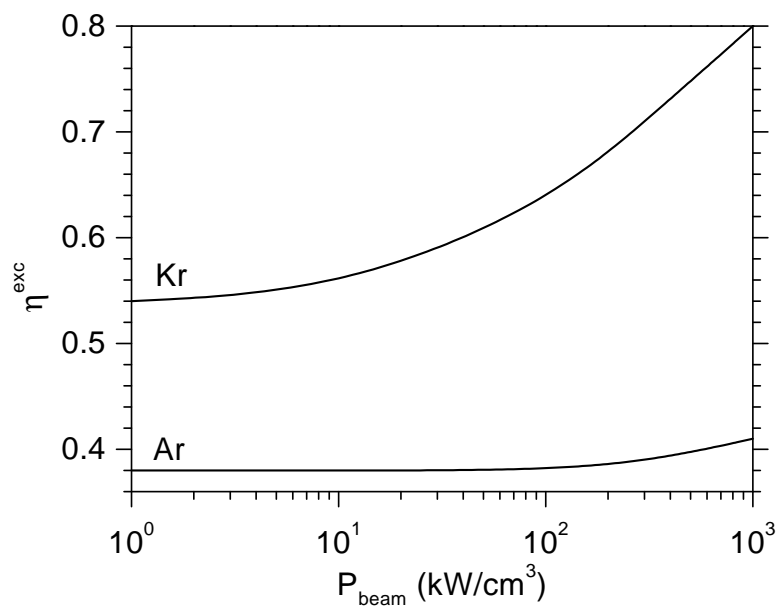


Fig. 11

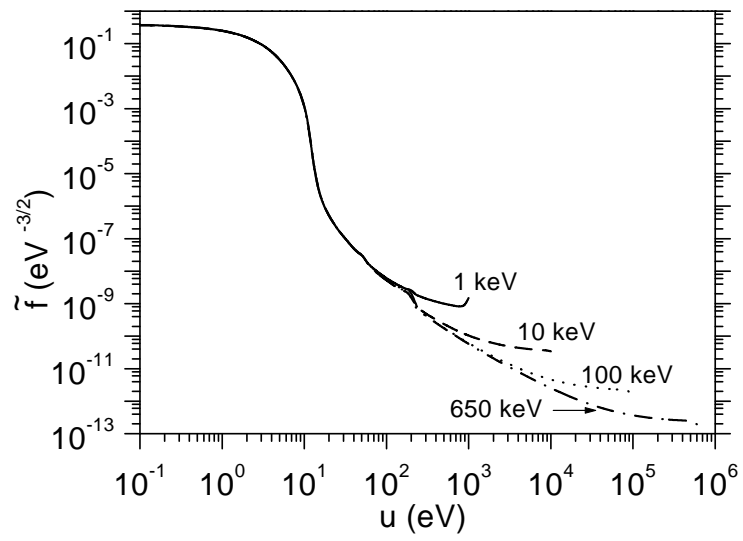


Fig. 12

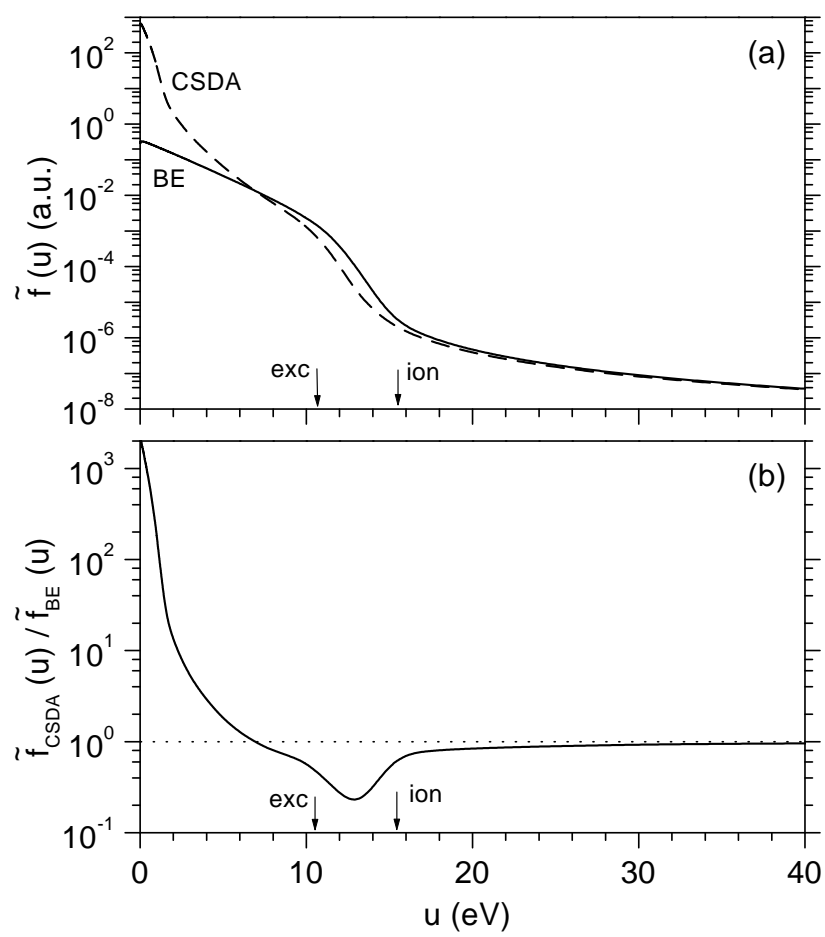


Fig. 13